(2)

MRC/WDC-R-097

MICROWAVE INTERACTION WITH AIR

Dean Pershing
W. Michael Bollen

June 1985

Prepared for: Naval Research Laboratory
4555 Overlook Avenue, SW
Washington, D. C. 20375

Attn. Dr. Michael Read
Code 4740

Purchase Order No: N00014-82-M-0262

MISSION RESEARCH CORPORATION
Capitol Building II, Suite 201
5503 Cherokee Avenue
Alexandria, Virginia 22312

Copy No. 4 MRC/WDC-R-097

MICROWAVE INTERACTION WITH AIR

Dean Pershing
W. Michael Bollen

June 1985

Prepared for: Naval Research Laboratory
4555 Overlook Avenue, SW
Washington, D. C. 20375

Attn: Dr. Michael Read
Code 4740

Purchase Order No: N00014-83-M-0262

MISSION RESEARCH CORPORATION
Capitol Building II, Suite 201
5503 Cherokee Avenue
Alexandria, Virginia 22312

CONTENTS

LIST OF FIGURES

LIST OF TABLES

MICROWAVE INTERACTION WITH AIR

I. INTRODUCTION

Microwave breakdown studies of gaseous elements have been carried out extensively over a wide range of pressures and for several microwave frequencies using CW and pulsed radiation sources[1]. The main emphasis in these studies was on the determination of the breakdown power threshold and its dependence on the gas pressure and the microwave frequency. The coupling of microwave energy into the breakdown plasma and neutral gas has not been studied in detail. The reason for this is that, until recently, no high-power microwave sources have been available to perform such studies. Most of the early work performed on breakdown thresholds was performed using high Q cavities to obtain the necessary electric field to break down the gas. Once breakdown of the gas occurred, the Q of the cavity dropped and the interaction changed. Using the NRL high-power gyrtron facility, we have been able to eliminate the need for cavities and have performed experiments using a focused geometry[2] to examine the coupling of microwave energy to nitrogen gas during breakdown. We have also modeled the experiments using a 1-D computer simulation code[3]. Simulations were performed in a spherical geometry using a self-consistent, nitrogen chemistry, wave optics, microwave breakdown simulation code, MINI.

The main emphasis of past work was on the ionization front created during nitrogen breakdown and its motion and plasma properties, as observed experimentally. This motion is not a movement of the plasma, but rather a movement of where the strongest ionization of the gas is taking place. We believe it to be due to two effects: 1) delayed ionization, and 2) reflection from the plasma itself. Since the electron density is proportional to e^{tI_o}, where I_o is the local microwave intensity, breakdown occurs faster in those regions of high intensity. In a focused system this results in breakdown beginning at the focus. The breakdown then moves back into the lower intensity region as time progresses. If nothing else is occurring, one would then observe a cone of plasma late in time. However, the plasma is both absorptive and reflective. The reflection results in standing wave patterns. Thus, peaks $\lambda/2$ apart are seen to grow in time. The first peak is $\lambda/4$ from the plasma surface. As the density increases in these peaks, they become reflective and absorptive, cutting off the microwave energy to peaks behind them. Again, the density grows as e^{atI_o} and, therefore, those peaks nearest the focus initially grow fastest. If only one peak were reflecting, we would expect $\lambda/2$ structure. However, all the peaks reflect and, therefore, we expect $\lambda/4$, the distance from the reflecting surface to the first electric field maximum, to occur as well. Thus, in the experiment we would expect a background plasma due to delayed ionization with $\lambda/2$ and $\lambda/4$ structures in it due to reflection. Reflection and absorption will also prevent microwave penetration, so we expect to see the plasma disappear behind the front of the ionization. This results in the appearance of motion. This motion may then occur as $\lambda/2$ or $\lambda/4$ jumps, since once these structures develop, the intensity at these points is larger due to reflection than the background intensity.

This ionization front motion strongly affects the coupling of microwave energy to the gas; it determines where the energy will be absorbed, since its high density does not allow microwave penetration. Also, since it is moving, it spreads the heating out in the gas. Motion towards the microwave source has been observed by Salisbury and Flint[4], and by Beust and Ford[5]. The velocities were much slower, however, $V \approx 3 \times 10^3$ cm/s for Salisbury and Flint's work, and $V \approx 600$ cm/s for Beust and Ford's work. Raizer[6] advanced a theoretical treatment for the microwave discharge propagation in high pressure air ($\approx$1Atm) to explain Beust and Ford's results under CW conditions. Other work by Scharfman, et al[7], observed that for low pressures the breakdown plasma became opaque to microwaves, thus preventing penetration. In the previous study, we observed the formation of the front, its motion, the prevention of microwave penetration, and measured the plasma density and electron temperature of the front. Good agreement was found between the experiment and the simulation model. This work is briefly reviewed in Section II.

II. EXPERIMENT

A. Purpose of the Experiment

MRC has participated in establishing an experimental air breakdown facility at NRL. In the past, a 35 GHz, 150 kW gyrotron was used. A 200 pps repetition rate and 2 μs pulse length were possible. Microwave pulse shape and power were very stable. Breakdown effects also seemed to be stable, thus allowing data to be taken over many pulses. The microwave power available, however, limited breakdown to a pressure of approximately 100 Torr. A newly developed 95 GHz, 1 MW, 13 μs pulse length gyrotron was to be made available as a microwave source for this facility and would allow breakdown of air at atmospheric pressure. The air breakdown program was to be completed by performing experiments at full atmospheric pressure. This would allow one to determine if any physical processes become important due to increased collision frequency. Further, the atmospheric pressure region is the one for which microwave weapons have been considered.

The experimental plan called for experiments to be performed to determine the microwave coupling to air at one atmosphere. In particular, emphasis was to be placed on determining if the ionization front behavior continues and, if so, how it varied with pressure. Further, a determination to see if the ionization front motion could be prevented was to be made. In order to observe the ionization fronts, high speed photography was planned. The plasma density and temperature were to be monitored. This was to be done using existing diagnostics developed by MRC for the NRL air breakdown facility and modified to improve their performance.

Since the planned research was an extension of previous work, the previous experiments and results are reviewed below.

B. Previous Experiments

The microwave energy coupling experiments were performed in dry nitrogen using one of the NRL 35 GHz, high power gyrotons[8]. This gyrotron is capable of 150 kW, 1 μsec pulses at 100 pps. The investigation, however, was performed with a microwave power ≈ 112 kW using S polarization. The nitrogen pressure was variable. The data presented is at a pressure of 25 Torr which corresponds to $\nu/\omega \approx 0.65$, where ν is the collision frequency for electron momentum transfer, and ω is the natural frequency of the microwave radiation. The microwave radiation is introduced into a test chamber using a conical horn with a focusing dielectric lens in front (see Figure 1). The lens has a focal length of 11.2 cm and a diameter of 7.62 cm. The focal spot is elliptical and has an approximate Gaussian distribution in intensity, with half widths of 1.5 cm and 1.1 cm. The 3dB focal spot area is approximately 1.7 cm^2. For 112 kW, this implies 33 kW/cm^2 average power inside the 3dB spot. Breakdown, without a reflecting surface, was observed to cease at $p \approx 75$ Torr for P = 112 kW. Theoretically, we calculate an average power of 27 kW/cm^2 is required for breakdown at 75 Torr in nitrogen. This is in reasonable agreement with an estimated intensity of 33 kW/cm^2. We have, however, ignored the gaussian spread and assumed an even distribution.

The breakdown experiments were performed with and without a metal surface at the focal point. The planar metal surface could be oriented perpendicular, 90°, or with an angle of 45° to the incident radiation. The metal surface serves to set up a standing wave pattern in front of the surface, resulting in 4 I_0 at the peaks, where I_0 is the intensity of the incident radiation. Also, a thin dielectric could be placed off the metallic surface. This was used in determining the cause of the plasma motion observed, and will be discussed later.

Observation of the plasma was done using a TRW framing/streaking camera. A 20 ns exposure time was used in the framing mode, and a 2 μs exposure time in the streaking mode. Due to the amount of light present, multiple exposures were required to obtain easily visible photographs. However, some single shot experiments were performed and showed that the results were reproducible shot-to-shot. The electron temperature and density were measured by using a nitrogen-helium gas mixture. In a pure nitrogen mixture, only second positive nitrogen bands were observable. By introducing helium, the 5876A line could be used with the nitrogen 3371A

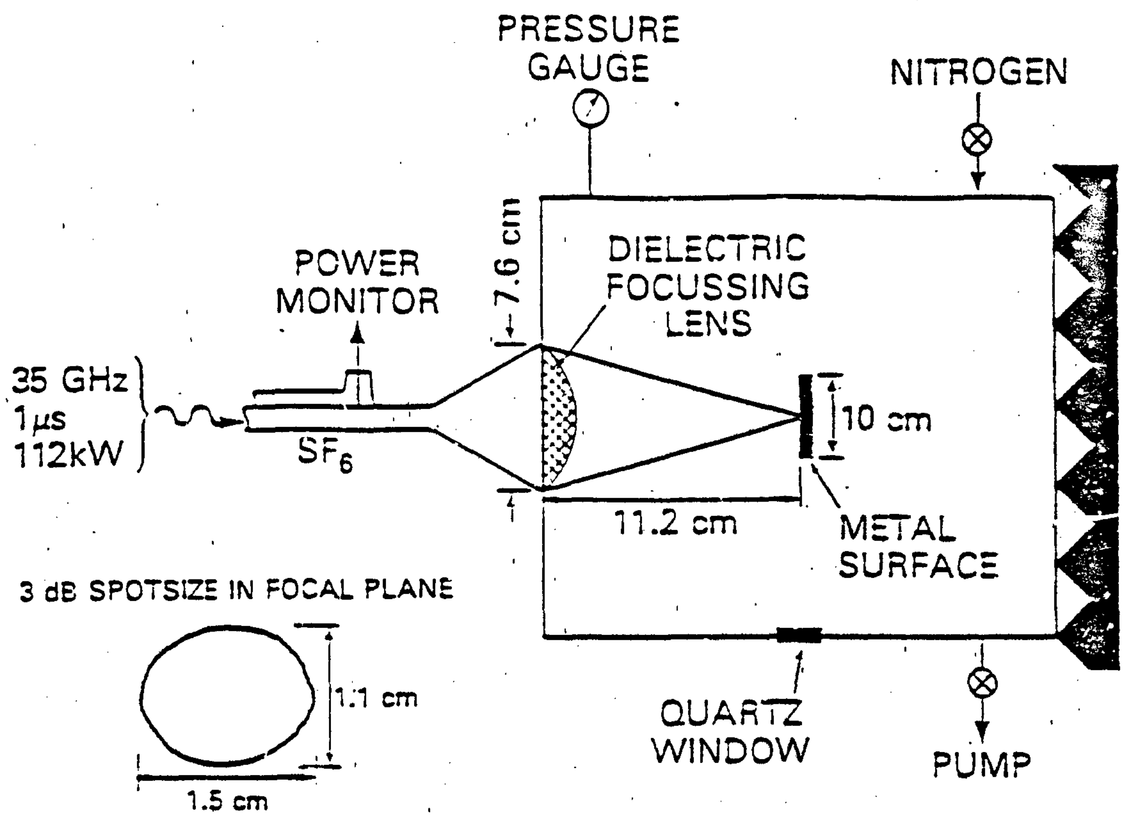

Figure 1. Schematic of nitrogen breakdown experiment.

band to make the required density and temperature measurements. An Oriel model 7240 monochrometer, f/3.7, with a 10Å bandwidth was used. The monochrometer output was measured using a 1P28 photomultiplier with a base modified for nano-second response time. Absolute intensity calibrations were performed using a calibrated deuterium arc lamp source[9] for 3371Å and a calibrated strip tungsten lamp source[10] for 5876Å.

Our experiments were performed at 25 Torr where we had approximately nine times the intensity required to break down the nitrogen at the focal spot. With the presence of a metal surface, a factor of four reduction in the power required for breakdown occurs due to the standing wave pattern which is set up. Due to the focused nature of the experiment, the standing wave pattern's intensity drops as the distance from the surface is increased. For the 45° target, in fact, there is only a small region of standing waves perpendicular to the surface. It is only for the 90° surface, or the case of a reflective plasma perpendicualr to the microwave beam, that a standing wave pattern back the length of the beam line exists. A delayed breakdown from the surface back towards the lens is then expected, since the growth of the plasma is proportional to e^{tI_0}. We believe that fluctuations in the reflective plasma surface and UV ionization (if any) will cause a smearing out of the standing wave pattern.

1. Time Resolved Photographs of Breakdown

The observed breakdown patterns for the three cases are shown in Figures 2 througn 4. In Figure 2, the breakdown without a surface is shown. A conical plasma is formed with its tail nearest the focal point and head towards the lens. This indicates that a large fraction of the microwave energy is concentrated on axis. For a diffraction limited spot size, we calculate the depth of field (where $I = I_0/e$) for our case to be 3.5 cm, which is approximately the length of the tail in the early breakdown region observed in Figure 2. The total length of the breakdown region is 5 cm. We calculate a length of 3.7 cm based on incident intensity decreasing to the nitrogen breakdown threshold as we move away from focus. This suggests reflection off the plasma must be occurring. We calcualte that ≈ 19% reflection would be required; the simulation suggests $R \geq 28\%$.

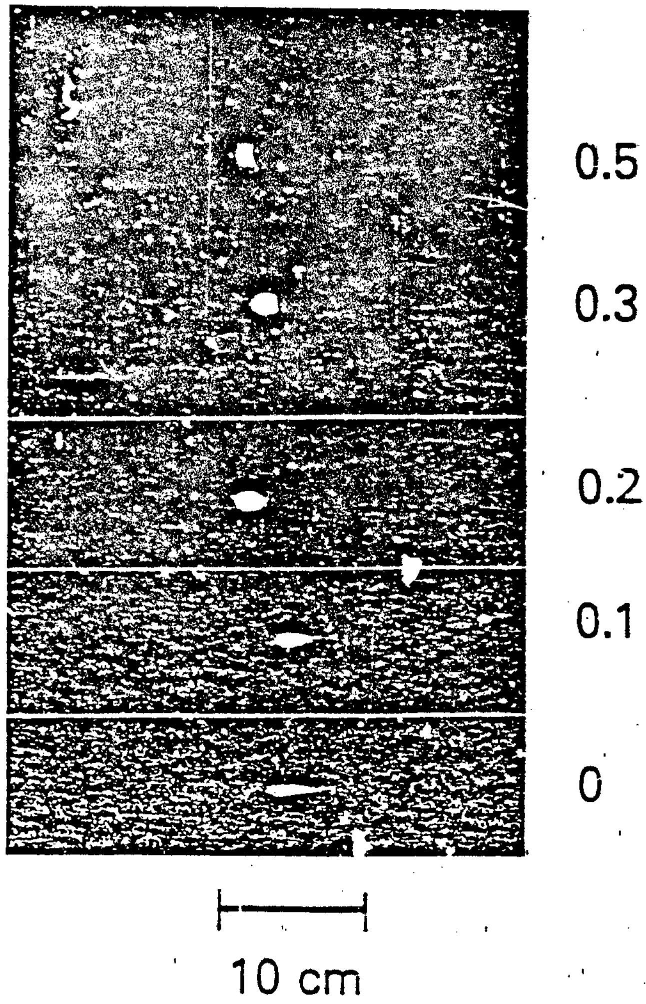

Figure 2. Framing photographs of breakdown at 25 Torr N_2 for no surface present, I_0 = 112 kW or 33 kW/cm^2 at focus. The microwaves are incident from the left. Frames are 100 ns apart and have a 20 ns exposure time. Time shown on right refers to the delay after the first observable breakdown and not the microwave pulse.

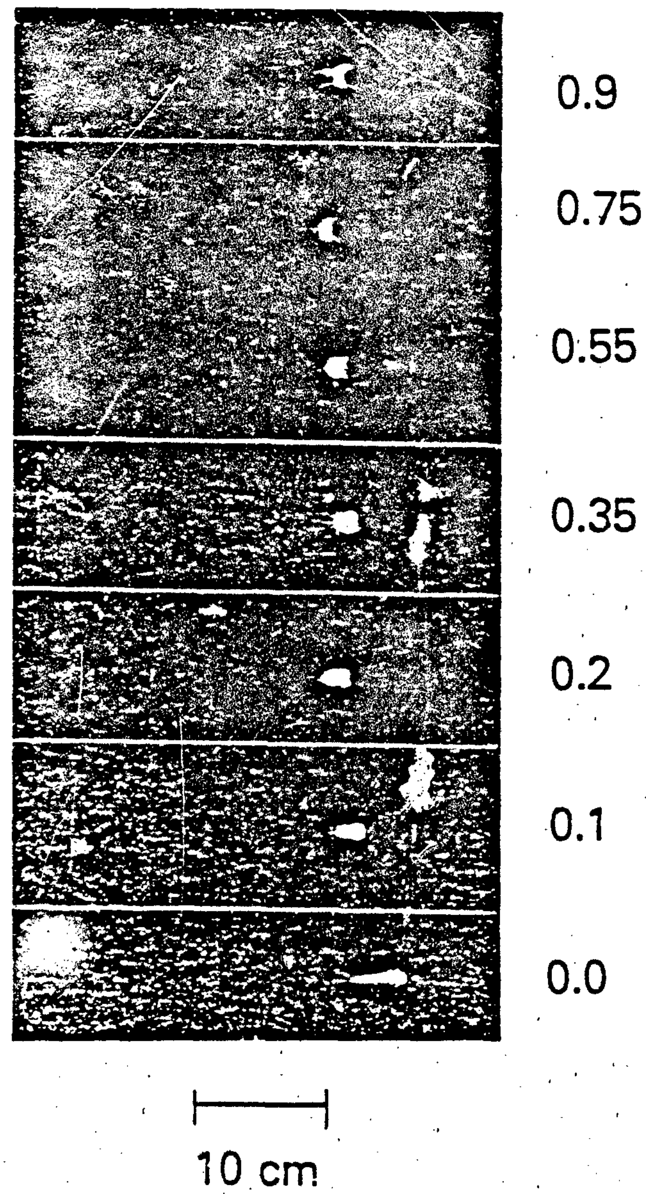

Figure 3a. Framing photographs at 25 Torr N_2 for 90° metal surface present at focus, I_0 = 112 kW. Times on right refer to the del[illegible] after first observable breakdown.

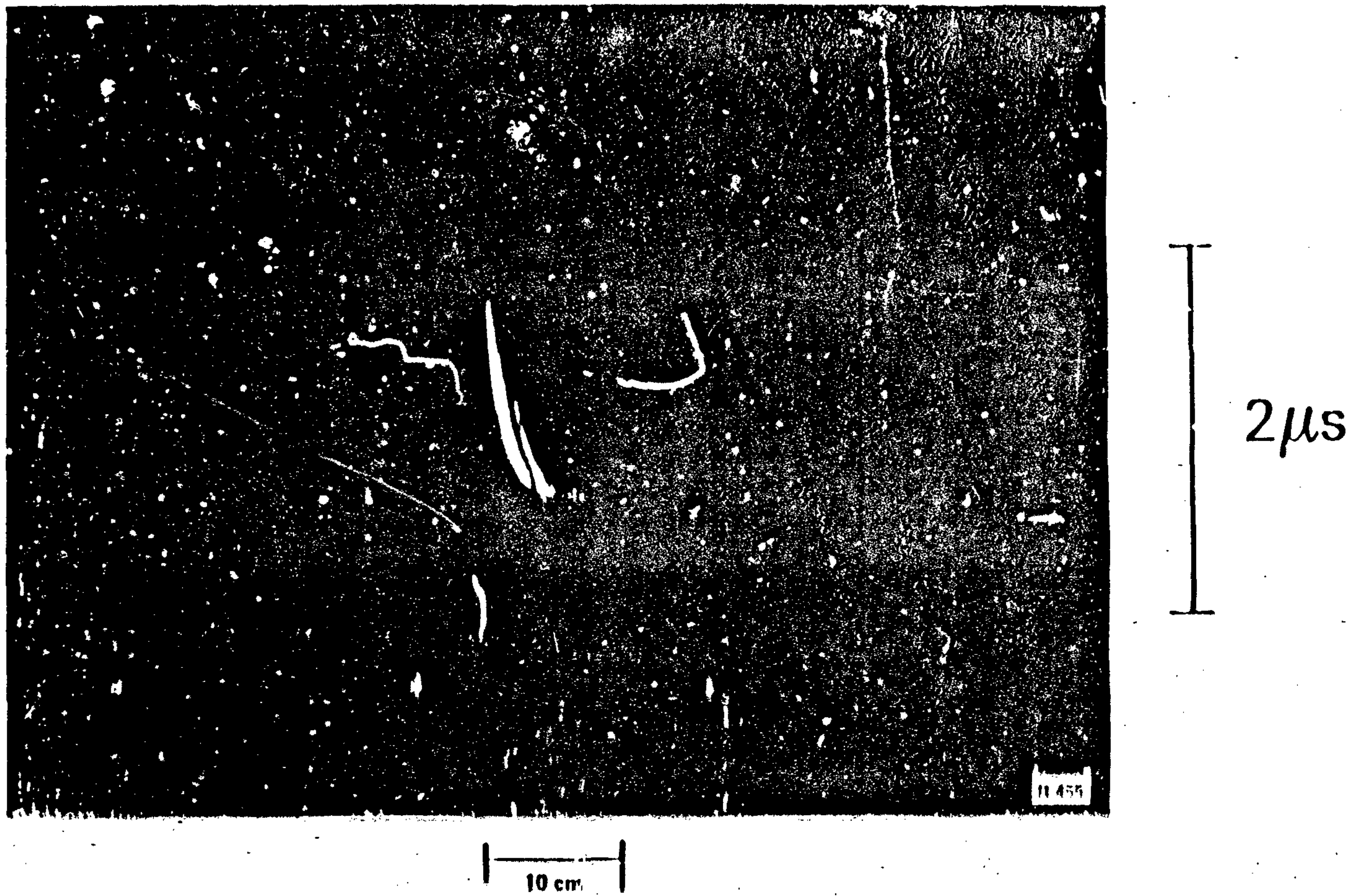

Figure 3b. Streaking photograph at 25 Torr H_2 for 90° metal surface present at focus, I_o = 112 kW. Streaking time was 2 µs. The velocity of motion for the ionization front is measured to be 4.6×10^6 cm/s from the photograph.

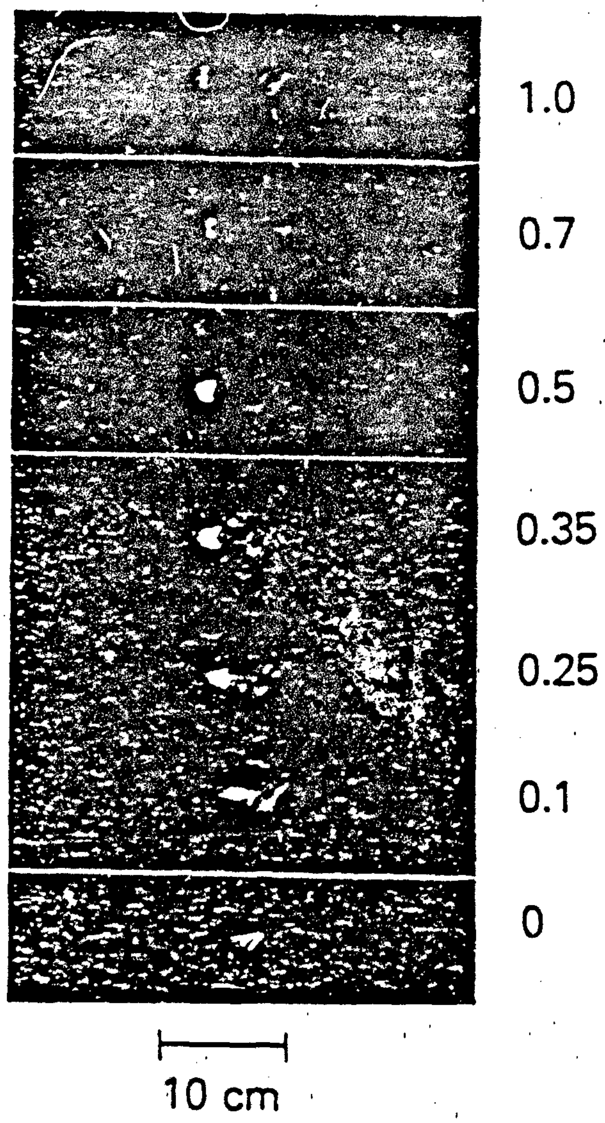

Figure 4. Framing photographs at 25 Torr N_2 for 45° metal surface, I_0 = 112 kW. Times shown on right refer to the delay after first observable breakdown.

The breakdown begins at the focal spot, but since the microwave power is above the breakdown threshold, a secondary breakdown region ahead of the focus forms in a time $\approx 2.4 \times 10^{-7}$s after the initial breakdown. As the electron density in this secondary breakdown region increases to $N_c = (\omega^2 + \nu^2)m_e/(4\pi e^2)$, the tail (focus) region disappears due to the microwaves being absorbed and reflected by the plasma at the head. Once the microwave energy is stopped from reaching the plasma in the tail, the plasma temperature there drops rapidly ($\tau \approx 10$ ns), and the emitted light ceases. The plasma itself also begins to decay, but on a longer time scale. Late in time, we see that a single absorbing layer about one wavelength thick is formed.

Figure 3a shows the framing camera data for the perpendicular surface experiment, and Figure 3b shows a streak photograph for the same case. We expect a standing wave to be set up off the surface with the first maximum $\lambda/4$ from the surface, and with the rest of the maxima spaced $\lambda/2$ apart. This can be seen in Figure 3a. Also observed is a "blooming" of the visible plasma near the target. We believe this is an effect due to the focusing. The microwave beam becomes more intense near focus. Therefore, the diameter of the beam capable of breaking down the plasma increases. Similar to the no-target case, an absorbing front travels away from the target towards the microwave source. From the displacement in the streak photograph, we calculate that the plasma moves away from the surface with a velocity $\approx 4.6 \times 10^6$ cm/s. It continues to move back along the microwave beam until the beam energy decreases sufficiently (due to defocusing) so that the heating with any reflected microwaves is below the breakdown threshold. This "stagnation point" is also observed for the 45° surface. Similar behavior is also observed in the computer simulation.

The 45° data is shown in Figure 4. It is similar to the 90° data, except fringes occur $\lambda/(2 \cos \theta)$ apart, $\theta = 45°$, with the first fringe at $\lambda/(4 \cos \theta)$ from the surface. Again, an absorbing front moving along the beam axis is observed. This occurs as a result of energy reflected by the plasma along the beam. Since we are far above threshold, we believe a planar plasma, perpendicular to the beam, grows near the target and is initiated by the plasma growth at the standing wave maxima. Its density grows ($N_e \rightarrow N_c$), and it becomes reflective, setting up standing waves. Plasma density builds at these maxima, cutting off microwave penetration, and the process repeats. Visually, this appears as plasma motion. We would expect the motion to jump in either $\lambda/2$ or $\lambda/4$ steps. Some of the 45° data shows $\lambda/2$ bars behind the main moving plasma. In general, however, this is not observed. The $\lambda/2$ spacing is at about the limit of resolution. Further, we believe that fluctuations in the reflective plasma surface cause a smearing out of the standing wave pattern and results in the more solid-like appearance we observe for the moving plasma.

One other possible explanation for the front motion is that UV emission causes ionization to occur in front of the plasma. This new plasma absorbs microwaves, heats up, and then the process repeats. This would result in a uniform smear with no $\lambda/2$ structure. Our data is somewhat suggestive of this. To check this idea, we placed a thin dielectric a few wavelengths off the metallic surface to stop UV penetration, but allow microwave transmission. If UV ionization were the method of propagation, we expected the plasma to stop moving when it hit the dielectric. The plasma moved through the dielectric barrier. We, therefore, believe the motion to be due to reflection from the plasma itself, resulting in ionization fronts. However, ionization due to UV may be responsible for some of the smearing of the $\lambda/2$ and $\lambda/4$ structure. The UV ionization mean free path is ≈ 0.05 cm $\ll \lambda/2$ for our conditions.

For the 45° target case, the breakdown was examined as the power was decreased. As the power was decreased, the ionization front was observed to stagnate closer and closer to the target, as expected. When the incoming power was 20 kW, ≈ 5.9 kW/cm^2, we observed only two fringes and no apparent ionization front. At 30 kW, the front reappeared. Incident radiation on a metal surface for breakdown to occur at 25 Torr is ≈ 0.75 kW/cm^2. However, the pressure was only twice the free nitrogen breakdown threshold of 3 kW/cm^2, and this will be the dominant threshold for ionization front travel due to delayed ionization.

2. Spectroscopic Measurement of Density and Temperature

In order to measure the temperature and density of the electrons, the absolute intensity of the nitrogen second positive band, 3371Å, was compared to the absolute intensity of the neutral helium line at 5876Å. A mixture of the helium and nitrogen was used to perform this experiment. The 3371Å band corresponds to the (0,0) transition in the second positive band system of N_2. We obtained the electron temperature from the ratio of the two lines[11] and the electron density from the absolute intensity measurement and the deduced electron temperature.

For an optically thin line, and assuming a steady state coronal model, the band intensity at 3371Å can be expressed as:

$$U_{u\ell} = \frac{N_e N_2 X_{oc} A_{o,o} E_{o,o} L}{A_o + q N_2} \quad (1)$$

where N_2 is the density of the nitrogen molecules in the ground state, X_{oc} is the emission excitation rate coefficient, $A_{o,o}$ is the transition rate for the band at 3371Å and A_o is the total transition rate for the excited state, $E_{o,o}$ is the photon energy, L is the length of the emitting plasma, and q is the quenching rate coefficient of the excited state by the neutral species. A similar equation can be written for the intensity of the helium line. The excitation rate coefficients for 3371Å and 5876Å were obtained using the measured cross sections[12,13] averaged over a Maxwellian electron velocity distribution. The transition rates for 3371Å and for 5876Å are from Refs. (14) and (15), respectively. The quenching rate coefficient[16] for 3371Å by N_2 is 1.15×10^{-11} cm^3/sec.

The measured absolute intensities of 3371Å and 5876Å in a mixture of 15 Torr N_2 and 19 Torr He were 25.36 W/cm^2sr and 5.6×10^{-2} W/cm^2sr. Using the above analysis, we obtain $T_e = 3.8$ eV and $N_e = 4.4 \times 10^{12}$ cm^{-3} for the average density over a 2 cm chord. If quenching of the helium line by nitrogen is included, the electron temperature changes slightly, T_e = 4.1 eV, with a corresponding slight decrease in the calculated electron density. This electron density is in reasonable agreement with Langmuir probe data, $N_e \sim 2 \times 10^{13}$ cm^{-3}, and simulation predictions, N_e = 3.6×10^{13} cm^{-3}, since these last two are peak local densities. It is reasonable to expect that the peak density is at least four times larger than the average density, since the density is proportional to $e^{I_0 t}$, and the microwave intensity is Gaussian across the chord. (The two centimeter chord is slightly larger than the FWHM of the intensity Gaussian.) A comparison of the absolute intensity of the 3371Å nitrogen band for pure N_2, as observed experimentally (I_{exp} = 1.12×10^{20} eV/(cm^2-s-sr)), agreed reasonably well with the simulation predictions for similar conditions (I_{sim} = 3.6×10^{20} eV/(s-cm^2-sr)). As expected, the simulation also predicted a lower electron temperature, $T_e \approx 3.25$ eV, for the pure N_2 case.

In conclusion, we have observed that for $I > I_B$, ionization fronts form and move towards the source at a velocity $\approx 4.6 \times 10^6$ cm/s. These ionization fronts result from both delayed ionization and reflection of microwave energy from the front. The front density can become quite large and is seen to cut off microwave penetration in about one wavelength in late time. The average chord plasma density was spectroscopically measured to be N_e = 4.4×10^{12} cm^{-3}, and the electron temperature to be T_e = 3.5 eV for a nitrogen-helium mixture. Langmuir probe measurements of the density gave reasonable agreement with peak densities for pure nitrogen of $N_e \approx 2 \times 10^{13}$ cm^{-3}. The cut-off of microwave penetration observed photographically suggests an electron density $N_e = N_c = 2.2 \times 10^{13}$ cm^{-3}. We expect the electron temperature in the gas mixture to be higher since N_2 vibrational and low-lying electronic states act to decrease T_e, and monoatomic H_e has no such states. Reasonable agreement was seen with the simulation for the velocity of the ionization front, N_e, T_e, and I_{3371}. The simulation predicts small reflection, R < 29%, and low gas temperature, $T_g \leq 0.027$ eV.

C. Present Experiment

Several modifications to the previous experimental set-up were planned to improve results. In particular, the photomultiplier tube used in the previous study was limited in its response to the 5876Å He line. A new tube was proposed to NRL for use to enhance the diagnostic sensitivity. The same streaking and framing set-up was planned for use and was recalibrated.

Unfortunately, a large difficulty arose after the plasma diagnostics were configured. The 1GW gyrotron tube was not available for use due to difficulties in getting the tube operational, and MRC began to assist in attempting to get the tube operational by participating in the gun design. These efforts are described in the next section. To date, the 1GW gyrotron has not been functional. All efforts to get the device functional at 1GW have failed.

III. SIMULATION OF THE GUN

A. Introduction

This section describes the results of computer calculations of electron trajectories performed in support of the gyrotron design effort at NRL. The goal of these calculations was to determine acceptable combinations of magnetic field profile, intermediate anode voltage, and anode voltage to place the electrons at the proper guiding center radius and with the proper transverse/axial velocity ratio (alpha) to maximize the gyrotron interaction with the TE_{13} waveguide mode. The code used in these calculations is SCRIBE[17], a version of the SLAC electron optics code originally written by W. Herrmansfeldt. The modifications in this version are due to R. H. Jackson of MRC.

B. Simulation Parameters

The simulations were performed within the following parameter context:

maximum anode voltage:	70kV
maximum interelectrode voltage:	35kV
beam current:	10A
desired alpha:	1.5
drift tube radius:	0.48cm
minimum magnetic field at cathode:	2.3kG
maximum coil current:	50A

The major parameter to be determined is the average electron guiding center radius. Since the gyrotron is designed to interact with the TE_{13} waveguide modes, the electrons must be placed at the proper radius for maximum interaction with this mode. It has been shown[18] that the interaction strength is proportional to the quantity $(J_{n-1}^2(x)+J_{n+1}^2(x))$, where J_m is the Bessel function of the first kind of order m and $x = k_{13}r/r0$; k_{13} = third root of the derivative of the first-order Bessel function, and r0 is the drift tube radius. A graph of $J_0^2+J_2^2$ for $0<r<.5$cm is shown in Figure 5. This graph shows that the maximum interaction strength between the TE_{13} mode and a hollow electron beam is at a radius of approximately 0.19cm. This is the desired average guiding center radius. Adiabatic considerations imply that a magnetic field compression ratio of approximately 12:1 (final=33.6kG:cathode=2.8kG) will place the electrons near the desired radius.

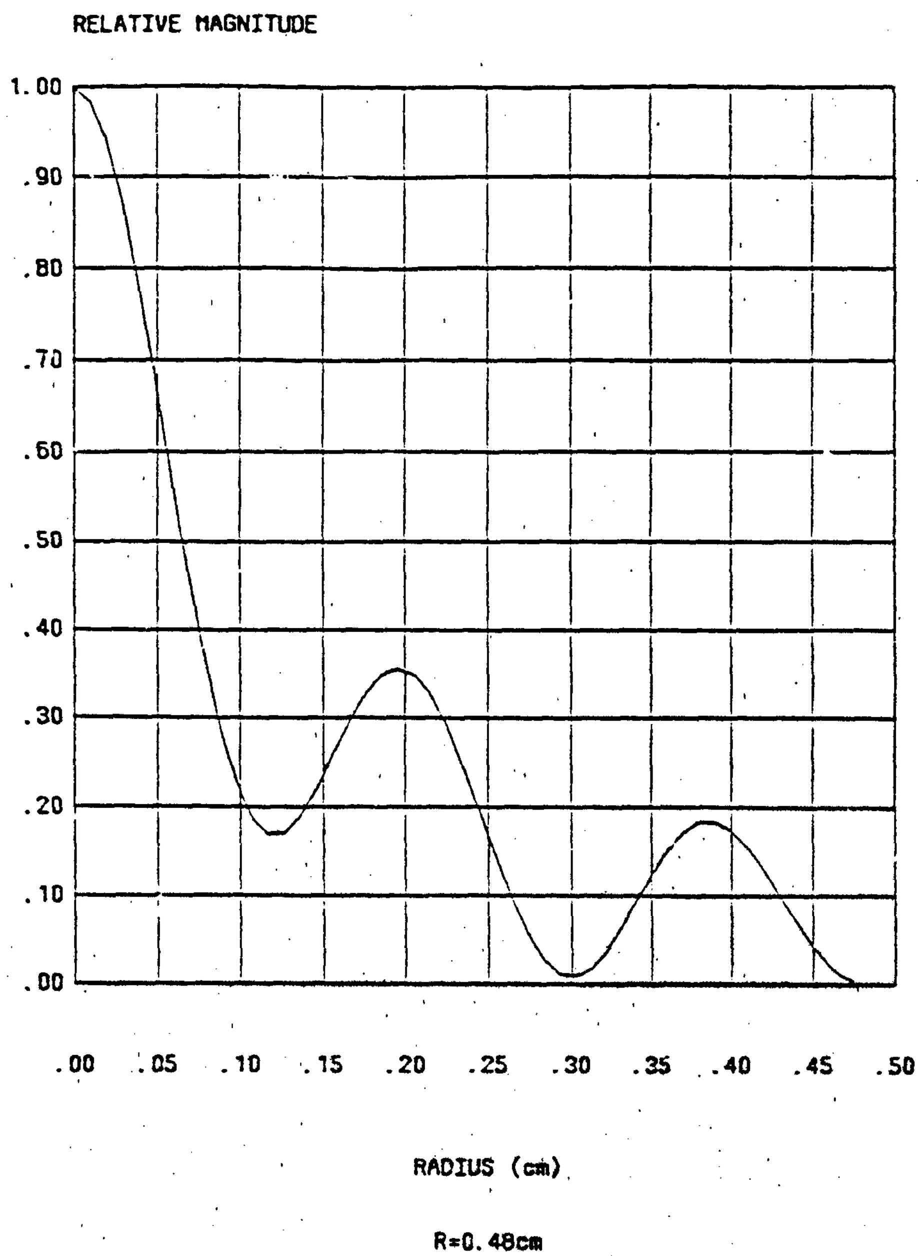

Figure 5. Gyrotron Interaction with TE13 Mode

C. Simulation Input Data

Boundary data for SCRIBE input were generated from a digitization of the electrode configuration as specified in the electron gun blueprint supplied to MRC by NRL. For the purposes of this simulation, the straight section of the anode was extended to permit trajectory calculations in the uniform magnetic field region. No other boundary or electrode shape changes were made. Please refer to the typical trajectory plots shown below for details of the simulation boundary.

The mesh sizes selected for this simulation were 1/2 and 1/4 mm/cell. Computation speed was, of course, faster with the coarser mesh, with results very close to those obtained with the fine mesh. The majority of the graphical results presented here were obtained using the 1/4mm mesh. A listing of the boundary input data for the 1/4mm mesh in the standard SLAC code format is given in Table 1.

Magnetic field data for this simulation were generated using a separate magnetic field code (EFFI[19]) that directly calculates the vector potential at any point in space due to an assembly of finite dimension coils. This approach is superior to the conventional method of first calculating the on-axis field due to an assembly of coils, and then using an expansion to calculate the field off-axis. The manufacturers' coil dimension and winding data were used in these calculations. A diagram of the individual coil positions in the same coordinate system used in the simulation is shown in Figure 6, with the trim coil identified. The approximate location of the cathode emitting surface is also indicated. A graph of a typical calculated axial magnetic field profile on-axis for the main coil assembly is shown in Figure 7, in this case driven at 45.41A. Also shown is the field profile (multiplied by -10) of the trim coil driven at 24.22A.

1	0	88	0.0000000	-0.1205978
1	1	88	2.0000000	-0.1401133
1	2	88	2.0000000	-0.1987534
1	3	88	2.0000000	-0.2967834
1	4	88	2.0000000	-0.4346695
1	5	88	2.0000000	-0.6130600
1	6	88	2.0000000	-0.8328171
1	7	87	-0.3439331	-0.0950699
1	8	87	2.0000000	-0.4011688
1	9	87	2.0000000	-0.7528000
1	10	86	-0.3665791	-0.1520081
1	11	86	2.0000000	-0.6012421
1	12	85	-0.1973543	-0.1034775
1	13	85	2.0000000	-0.6623383
1	14	84	-0.4426394	-0.2822495
1	15	84	2.0000000	-0.9686584
1	16	83	-0.9566746	-0.7284164
1	17	82	-0.6659489	-0.5702286
1	18	81	-0.5271397	-0.5054626
1	19	80	-0.5121536	-0.5493393
1	20	79	-0.6015953	-0.7230759
1	21	78	-0.7812042	2.0000000
1	21	77	-0.0005331	-0.0577621
1	22	76	-0.3713417	-0.6023331
1	23	75	-0.7671757	2.0000000
1	23	74	-0.2228603	-0.4424591
1	24	73	-0.7341957	2.0000000
1	24	72	-0.2977371	-0.7578125
1	25	71	-0.9106483	2.0000000
1	25	70	-0.5705814	2.0000000
1	25	69	-0.2755966	2.0000000
1	25	68	-0.0240970	-0.1056976
1	26	67	-0.8147793	2.0000000
1	26	66	-0.6359291	2.0000000
1	26	65	-0.4596920	2.0000000
1	26	64	-0.2830549	2.0000000
1	26	63	-0.1072178	-0.6083755
1	27	62	-0.9309807	2.0000000
1	27	61	-0.7547436	2.0000000
1	27	60	-0.5785065	2.0000000
1	27	59	-0.4022694	2.0000000
1	27	58	-0.2260323	2.0000000
1	27	57	-0.0497952	-0.2825470
1	28	56	-0.8735580	2.0000000
1	28	55	-0.6973209	2.0000000
1	28	54	-0.5210838	2.0000000
1	28	53	-0.3448467	2.0000000
1	28	52	-0.1686096	-0.9567223
1	29	51	-0.9923725	2.0000000
1	29	50	-0.8161354	2.0000000
1	29	49	-0.6398983	2.0000000
1	29	48	-0.4636612	2.0000000
1	29	47	-0.2874241	2.0000000
1	29	46	-0.1111870	-0.6308937
1	30	45	-0.9349499	2.0000000
1	30	44	-0.7587128	2.0000000
1	30	43	-0.5824757	2.0000000
1	30	42	-0.4062386	2.0000000
1	30	41	-0.2300014	2.0000000
1	30	40	-0.0537643	-0.3050652
1	31	39	-0.8775272	2.0000000
1	31	38	-0.7012901	2.0000000
1	31	37	-0.5250540	2.0000000
1	31	36	-0.3488159	2.0000000
1	31	35	-0.1725788	-0.9792404
1	32	34	-0.9963417	2.0000000
1	32	33	-0.8201046	2.0000000
1	32	32	-0.7200000	2.0000000
1	32	31	-0.7200000	2.0000000
1	32	15	-0.7200000	2.0000000
1	32	1	-0.7200000	2.0000000
1	32	0	-0.7200000	2.0000000
0	34	0	2.0000000	0.0000000
0	35	0	2.0000000	0.0000000
0	45	0	2.0000000	0.0000000
0	53	0	2.0000000	0.0000000
4	54	0	0.5320000	0.0000000
4	54	1	0.5320000	2.0000000
4	54	15	0.5320000	2.0000000
4	54	32	0.5320000	2.0000000
4	54	33	0.5320000	2.0000000
4	54	34	0.3580284	2.0000000
4	54	35	0.1812286	2.0000000
4	54	36	0.0044289	0.0250549
4	53	37	0.8276291	2.0000000
4	53	38	0.6508331	2.0000000
4	53	39	0.4740334	2.0000000
4	53	40	0.2972336	2.0000000
4	53	41	0.1204338	0.6811981
4	52	42	0.9436378	2.0000000
4	52	43	0.7668381	2.0000000
4	52	44	0.5900383	2.0000000
4	52	45	0.4132385	2.0000000
4	52	46	0.2364388	2.0000000
4	52	47	0.0596428	0.3373413
4	51	48	0.8828430	2.0000000
4	51	49	0.7060432	2.0000000
4	51	50	0.5292435	2.0000000
4	51	51	0.3524475	2.0000000
4	51	52	0.1756477	0.9934845
4	50	53	0.9988480	2.0000000
4	50	54	0.8220482	2.0000000
4	50	55	0.6452484	2.0000000
4	50	56	0.4684525	2.0000000
4	50	57	0.2916527	2.0000000
4	50	58	0.1148529	0.6496277
4	49	59	0.9340531	2.0000000
4	49	60	0.7612572	2.0000000
4	49	61	0.5840574	2.0000000
4	49	62	0.4076576	2.0000000
4	49	63	0.2308576	2.0000000
4	49	64	0.0540581	0.3057709
4	48	65	0.8772621	2.0000000
4	48	66	0.7004623	2.0000000
4	48	67	0.5760000	2.0000000
4	48	68	0.5760000	2.0000000
4	48	100	0.5760000	2.0000000
4	48	130	0.5750000	2.0000000
4	48	131	0.5760000	2.0000000
4	49	132	2.0000000	-0.6840000
4	59	132	2.0000000	-0.6840000
4	60	132	2.0000000	-0.6840000
4	68	132	2.0000000	-0.6840000
4	69	132	0.0000000	-0.6840000
0	69	133	0.0000000	2.0000000
0	69	134	0.0000000	2.0000000
0	69	150	0.0000000	2.0000000
0	69	167	0.0000000	2.0000000
2	69	168	0.0000000	0.5200000
2	68	168	2.0000000	0.5200000
2	55	168	2.0000000	0.5200000
2	43	168	2.0000000	0.5200000
2	42	168	2.0000000	0.5200000
2	41	168	2.0000000	0.5525360
2	40	168	2.0000000	0.7459564
2	39	169	0.2848473	0.1313171
2	38	169	2.0000000	0.7557526
2	37	170	0.7042732	0.7383728
2	36	171	0.7999992	2.0000000
2	36	172	0.5418549	2.0000000
2	36	173	0.2837067	2.0000000
2	36	174	0.0255623	0.0990295
2	35	175	0.7674179	2.0000000
2	35	176	0.5092697	2.0000000
2	35	177	0.2511253	0.9728088
2	34	178	0.9929810	2.0000000
2	34	179	0.7348366	2.0000000
2	34	180	0.47[illegible]	2.0000000
2	34	181	0.2185440	0.8465881
2	33	182	0.9603996	2.0000000
2	33	183	0.7022514	2.0000000
2	33	184	0.4441071	2.0000000
2	33	185	0.1859627	0.7203674
2	32	186	0.9278145	2.0000000
2	32	187	0.6696701	2.0000000
2	32	188	0.4115257	2.0000000
2	32	189	0.1533775	0.5941620
2	31	190	0.8952332	2.0000000
2	31	191	0.6370888	2.0000000
2	31	192	0.4268396	2.0000000
2	31	193	0.3597532	2.0000000
2	31	194	0.2906666	2.0000000
2	31	195	0.2225780	2.0000000
2	31	196	0.1544914	2.0000000
2	31	197	0.0864048	2.0000000
2	31	198	0.0183182	0.2690830
2	30	199	0.9582316	2.0000000
2	30	200	0.8921449	2.0000000
2	30	201	0.8180564	2.0000000
2	30	202	0.7859698	2.0000000

Table 1. Scribe Boundary Input Data For Gyrotron Gun

2,	30,203,	0.6778831,	2.0000000
2,	30,204,	0.6097965,	2.0000000
2,	30,205,	0.5417099,	2.0000000
2,	30,206,	0.4736233,	2.0000000
2,	30,207,	0.4055347,	2.0000000
2,	30,208,	0.3374481,	2.0000000
2,	30,209,	0.2693615,	2.0000000
2,	30,210,	0.2012749,	2.0000000
2,	30,211,	0.1331882,	2.0000000
2,	30,212,	0.0651016,	0.9561462
2,	29,213,	0.9970150,	2.0000000
2,	29,214,	0.9289265,	2.0000000
2,	29,215,	0.8608398,	2.0000000
2,	29,216,	0.7927532,	2.0000000
2,	29,217,	0.7246666,	2.0000000
2,	29,218,	0.6565800,	2.0000000
2,	29,219,	0.5884933,	2.0000000
2,	29,220,	0.5204046,	2.0000000
2,	29,221,	0.4523182,	2.0000000
2,	29,222,	0.3842316,	2.0000000
2,	29,223,	0.3161449,	2.0000000
2,	29,224,	0.2480583,	2.0000000
2,	29,225,	0.1799717,	2.0000000
2,	29,226,	0.[illegible]18851,	2.0000000
2,	29,227,	0.0437965,	0.6432495
2,	28,228,	0.9757099,	2.0000000
2,	28,229,	0.9076233,	2.0000000
2,	28,230,	0.8395367,	2.0000000
2,	28,231,	0.7714500,	2.0000000
2,	28,232,	0.7033634,	2.0000000
2,	28,233,	0.6352749,	2.0000000
2,	28,234,	0.5671883,	2.0000000
2,	28,235,	0.4991016,	2.0000000
2,	28,236,	0.4310150,	2.0000000
2,	28,237,	0.3629284,	2.0000000
2,	28,238,	0.2948418,	2.0000000
2,	28,239,	0.2267551,	2.0000000
2,	28,240,	0.1586666,	2.0000000
2,	28,241,	0.0905800,	2.0000000
2,	28,242,	0.0224934,	0.3303680
2,	27,243,	0.9544067,	2.0000000
2,	27,244,	0.8863201,	2.0000000
2,	27,245,	0.8182335,	2.0000000
2,	27,246,	0.7501450,	2.0000000
2,	27,247,	0.6820583,	2.0000000
2,	27,248,	0.6139717,	2.0000000
2,	27,249,	0.5458851,	2.0000000
2,	27,250,	0.4777985,	2.0000000
2,	27,251,	0.4097118,	2.0000000
2,	27,252,	0.3416252,	2.0000000
2,	27,253,	0.2735367,	2.0000000
2,	27,254,	0.2054501,	2.0000000
2,	27,255,	0.1373634,	2.0000000
2,	27,256,	0.0692766,	2.0000000
2,	27,257,	0.0011902,	0.0174866
2,	26,258,	0.9331036,	2.0000000
2,	26,259,	0.8650150,	2.0000000
2,	26,260,	0.7969284,	2.0000000
2,	26,261,	0.7288418,	2.0000000
2,	26,262,	0.6607552,	2.0000000
2,	26,263,	0.5926685,	2.0000000
2,	26,264,	0.5245819,	2.0000000
2,	26,265,	0.4564953,	2.0000000
2,	26,266,	0.3884068,	2.0000000
2,	26,267,	0.3203201,	2.0000000
2,	26,268,	0.2522335,	2.0000000
2,	26,269,	0.1841469,	2.0000000
2,	26,270,	0.[illegible]160603,	2.0000000
2,	26,271,	0.0479736,	0.7005898
2,	25,272,	0.9798851,	2.0000000
2,	25,273,	0.9117985,	2.0000000
2,	25,274,	0.8437119,	2.0000000
2,	25,275,	0.7756252,	2.0000000
2,	25,276,	0.7075386,	2.0000000
2,	25,277,	0.6394520,	2.0000000
2,	25,278,	0.5713[illegible]34,	2.0000000
2,	25,279,	0.503[illegible]68,	2.0000000
2,	25,280,	0.4351902,	2.0000000
2,	25,281,	0.3671036,	2.0000000
2,	25,282,	0.2990170,	2.0000000
2,	25,283,	0.2309303,	2.0000000
2,	25,284,	0.1628437,	2.0000000
2,	25,285,	0.0947552,	2.0000000
2,	25,286,	0.0266685,	0.3916931
2,	24,287,	0.9585819,	2.0000000
2,	24,288,	0.8904953,	2.0000000
2,	24,289,	0.8224087,	2.0000000
2,	24,290,	0.754322[illegible],	2.0000000
2,	24,291,	0.6862335,	2.0000000
2,	24,292,	0.6181469,	2.0000000
2,	24,293,	0.5500603,	2.0000000
2,	24,294,	0.481973[illegible],	2.0000000
2,	24,295,	0.4138870,	2.0000000
2,	24,296,	0.3458004,	2.0000000
2,	24,297,	0.2777138,	2.0000000
2,	24,298,	0.2096252,	2.0000000
2,	24,299,	0.1415386,	2.0000000
2,	24,300,	0.0734520,	2.0000000
2,	24,301,	0.0053654,	0.0787964
2,	23,302,	0.9372787,	2.0000000
2,	23,303,	0.8691921,	2.0000000
2,	23,304,	0.8011036,	2.0000000
2,	23,305,	0.7330170,	2.0000000
2,	23,306,	0.6649303,	2.0000000
2,	23,307,	0.5968437,	2.0000000
2,	23,308,	0.5287571,	2.0000000
2,	23,309,	0.4606705,	2.0000000
2,	23,310,	0.3925838,	2.0000000
2,	23,311,	0.3244953,	2.0000000
2,	23,312,	0.2564087,	2.0000000
2,	23,313,	0.1883221,	2.0000000
2,	23,314;	0.1202354,	2.0000000
2,	23,315,	0.0521488,	0.7658997
2,	22,316,	0.9840622,	2.0000000
2,	22,317,	0.9159756,	2.0000000
2,	22,318,	0.8478870,	2.0000000
2,	22,319,	0.7798004,	2.0000000
2,	22,320,	0.7117138,	2.0000000
2,	22,321,	0.6436272,	2.0000000
2,	22,322,	0.5755405,	2.0000000
2,	22,323,	0.5074539,	2.0000000
2,	22,324,	0.4393654,	2.0000000
2,	22,325,	0.3712788,	2.0000000
2,	22,326,	0.3031921,	2.0000000
2,	22,327,	0.2351055,	2.0000000
2,	22,328,	0.1670189,	2.0000000
2,	22,329,	0.0989323,	2.0000000
2,	22,330,	0.0308437,	0.4530029
2,	21,331,	0.9627571,	2.0000000
2,	21,332,	0.8946705,	2.0000000
2,	21,333,	0.8265839,	2.0000000
2,	21,334,	0.7584972,	2.0000000
2,	21,335,	0.6904106,	2.0000000
2,	21,336,	0.6223240,	2.0000000
2,	21,337,	0.5542355,	2.0000000
2,	21,338,	0.4861488,	2.0000000
2,	21,339,	0.4180622,	2.0000000
2,	21,340,	0.3499756,	2.0000000
2,	21,341,	0.2818890,	2.0000000
2,	21,342,	0.2680000,	2.0000000
2,	21,343,	0.2680000,	2.0000000
2,	21,410,	0.2680000,	2.0000000
2,	21,517,	0.2680000,	2.0000000
2,	21,518,	0.2680000,	0.0000000
0,	20,518,	2.0000000,	0.0000000
0,	19,518,	2.0000000,	0.0000000
0,	10,518,	2.0000000,	0.0000000
0,	5,518,	2.0000000,	0.0000000
0,	2,518,	2.0000000,	0.0000000
0,	1,518,	2.0000000,	0.0000000
0,	0,518,	0.0000000,	0.0000000
0,	0,517,	0.0000000,	2.0000000
0,	0,516,	0.0000000,	2.0000000
0,	0,360,	0.0000000,	2.0000000
0,	0, 90,	0.0000000,	2.0000000
0,	0, 89,	0.0000000,	2.0000000

Figure 1. Scribe Boundary Input Data for Gyrotron Gun (1/4mm MESH) (Cont.)

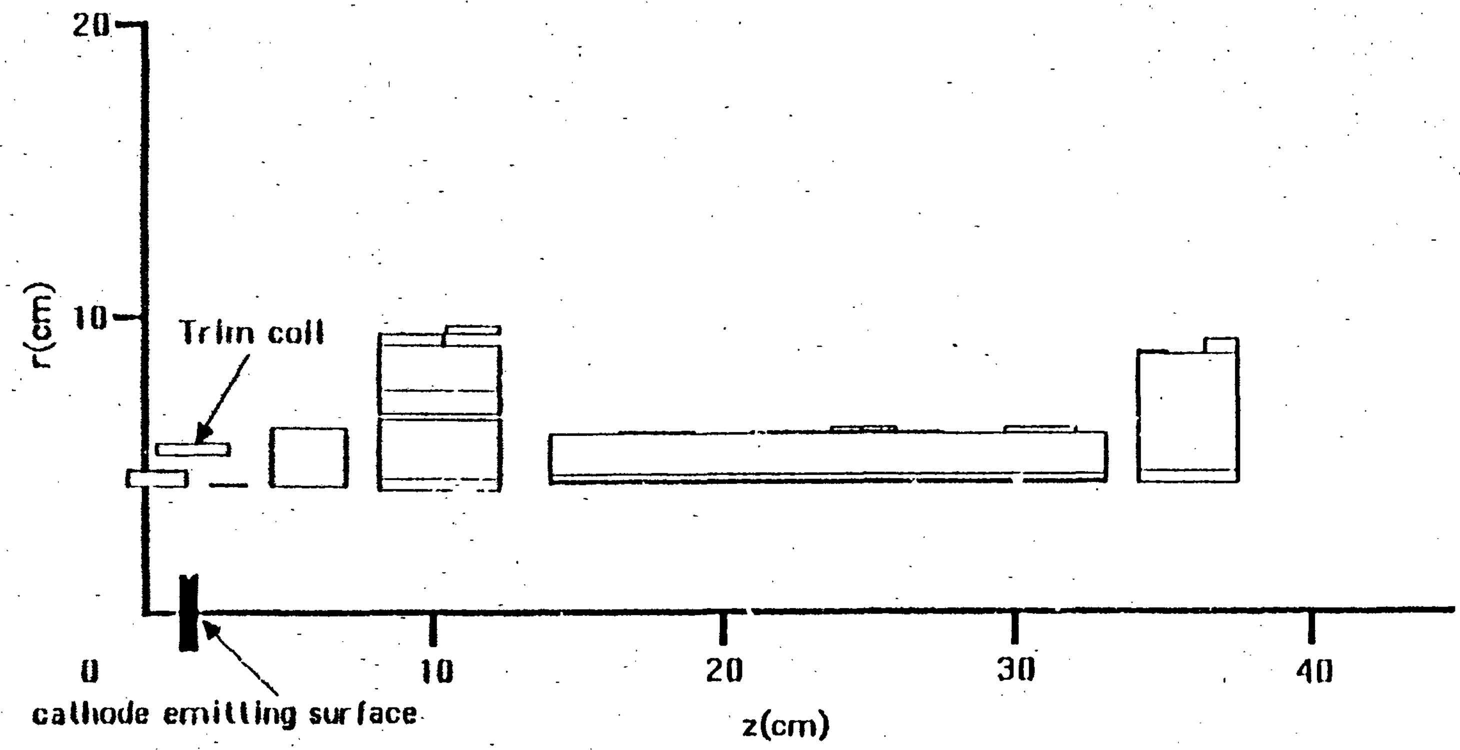

Figure 6. Coil Positions

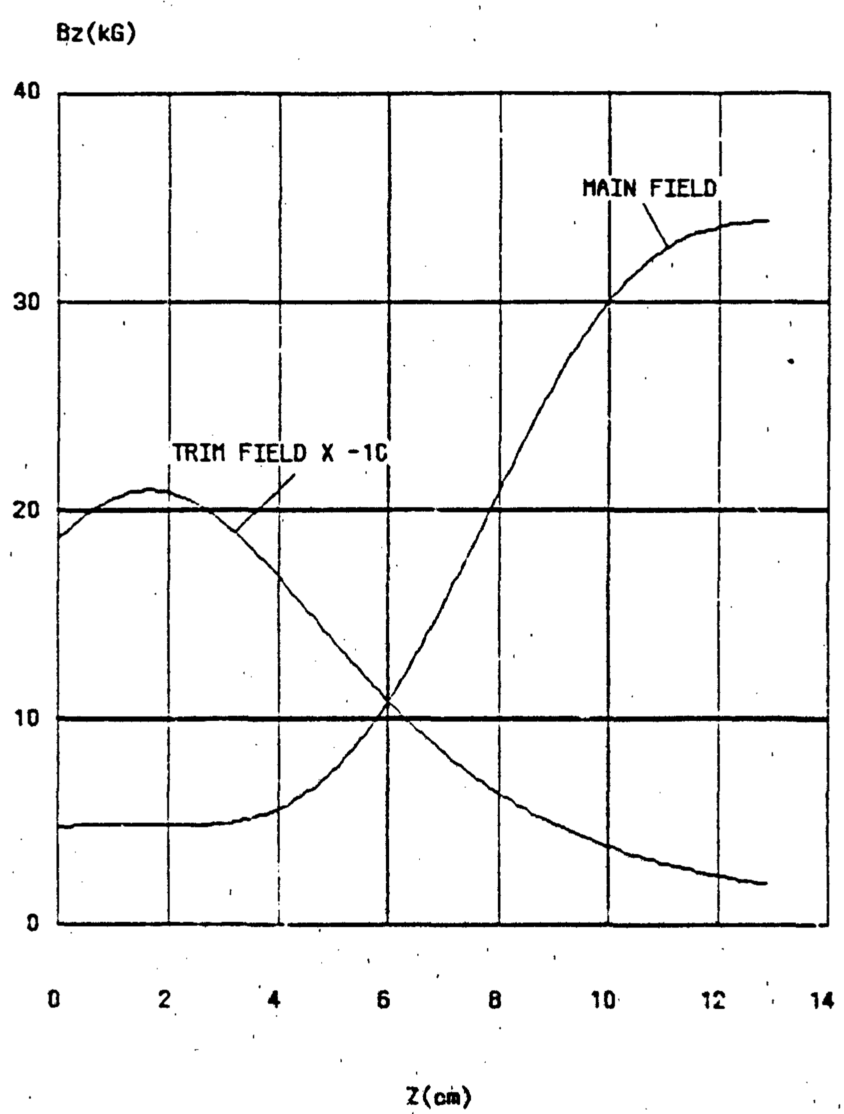

Figure 7. Axial Magnetic Field - Magnet Two

D. Results

As mentioned earlier, the simulations reported here were conducted with the goal of determining consistent sets of gun parameters for the successful operation of the high-power gyrotron now under design at NRL for air breakdown experiments. This was not to be a gun design exercise, and no changes in the electrode shapes were made. In addition, extensive simulations to determine parameter sensitivity around any one particular operating point were not attempted.

Within the context of the parameter constraints listed in Section III.B. above, the simulation results are summarized in Table 2. The notation for the table headings is as follows:

SCRRUN	SCRIBE run identification no.
V	anode voltage (kV)
VMOD	intermediate anode voltage (kV)
BZA-K	on-axis axial magnetic field at cathode axial locaton (kG)
BZA-F	on-axis axial magnetic field in uniform field region (kG)
ALPHA	transverse/axial velocity ratio
R G-C	average guiding center radius (cm)
BETA SP.	spread in relativistic factor beta (%)

The table entries are listed in the following order: 1-decreasing accelerating voltage (anode voltage); for each accelerating voltage, 2-decreasing magnetic field at cathode; 3-decreasing mod or intermediate anode voltage. Based on the criteria listed above, several parameter sets have been selected as possible gun operating points. These are indicated in Table 2 by asterisks (*). Those simulations using the 1/4mm mesh are indicated by NOTE 5.

The gun perveance is fixed in these simulations to model temperature-limited emission at 10A. However, two runs (11,12) were made at reduced perveance to simulate emission at 5.95 and 7.94A, respectively.

SCRUN.	V	VMOD	BZA-K	BZA-F	ALPHA	R G-C	BETA SP.	NOTE
9	71	35	3.73	33.66	.473	.241	1.6	
10	71	35	2.9	33.59	.762	.205	7.6	
96	70	35	2.81	33.34	.839	.204	4.4	1
95	70	35	2.76	33.57	.875	.197	4.5	
93	70	37.1	2.76	33.57	.832	.199	5	
* 81	70	37	2.5	33.55	1.39	.188	3.31	2
* 80	70	35	2.5	33.55	1.13	.191	3.21	2
* 6	70	33.05	2.37	33.54	1.24	.171	3.9	
* 2	70	33	2.37	33.54	1.24	.17	4.2	
* 78	70	35	2.3	33.53	2.31	.167	2.56	2
* 79	70	32.9	2.3	33.53	1.51	.179	5.81	2
* 83	67	35	2.5	33.55	1.21	.196	4.09	5
* 84	67	35	2.45	33.54	1.39	.193	4.48	5
* 85	67	35	2.4	33.54	1.65	.189	5.29	5
11	65	35	2.9	33.59	.77	.174	9.6	3
82	65	34	2.5	33.55	1.1	.191	3.28	2
14	60	35	3.17	33.61	.791	.214	5.1	
13	60	35	2.9	33.59	.849	.2	12.4	
12	60	35	2.9	33.59	.855	.2	11.8	4
* 60	60	35	2.37	33.54	2.16	.185	4.45	5
* 63	60	34	2.37	33.54	1.81	.186	4.23	5
* 61	60	33	2.37	33.54	1.64	.188	6.3	5
* 62	60	32	2.37	33.54	1.39	.189	6	5
* 24	60	30.5	2.37	33.54	1.13	.174	4.2	
20	60	30	2.37	33.54	1.06	.18	4.3	
46	60	30	2.37	33.54	1.08	.186	5.8	5
* 77	60	30.5	2.3	33.53	1.39	.179	4.72	2
* 75	60	30	2.3	33.53	1.27	.18	5.1	2
* 76	60	30	2.3	33.53	1.3	.157	6.83	5

* - POSSIBLE OPERATING POINT

Notes:

1 - Slight Origin Shift for Magnetic Field
2 - Step Size Halved
3 - 8.95A
4 - 7.94A
5 - Twice Original Resolution (1/4mm)

Table 2. Simulation Results

The gun performance does not appear to be extremely sensitive to the relative positions of the gun and coil systems, as evidenced by a comparison of runs 95 and 96. The coil system was shifted axially by approximately 0.9cm between runs 95 and 96. With the exception of run 96, the magnetic field at the z coordinate of the emission surface scales as Bz(kG) = -0.8558 I(A) + 4.8081, where I is the trim coil current and with the main coil current fixed at 45.41A.

Representative trajectory and trajectory with equipotential plots from these simulations, including both the 1/2 and 1/4mm meshes, are shown in Figures 6 - 15. These plots are presented in the same order as listed in Table 2. Since azimuthal symmetry is assumed for these simulations, only the first quadrant of the electron gun is shown. The positions of the cathode, intermediate anode, and anode are indicated in Figure 8. Note that the "R" axis scale is approximately 5.6 times that for the "Z" axis scale for enhanced visual clarity. The scales for both axes are in mesh units. Six trajectories are followed with the 1/2mm mesh, and ten are followed with the 1/4mm mesh. The electron emission takes place approximately 1.5 cells from the actual emission surface. The approximate center of the actual emission surface is located at (0.8cm, 1.1cm).

Although simulations of the full parameter matrix were not made, enough data exists to demonstrate several trends. The most important parameters for successful gyrotron operation are alpha and the average guiding center radius. The variation of alpha with the intermediate anode voltage for constant anode voltage and magnetic field is shown in Figure 16. In this case, V=60kV, the magnetic field at the cathode is 2.37 kG, and the final magnetic field is 33.54 kG. Although typical power supply construction does not allow a continuous variation of the intermediate anode voltage, one can see that this would be a convenient 'knob' to turn to adjust alpha. Under the same conditions as in effect for Figure 16, relatively small variations in intermediate anode voltage do not have a significant effect on the average guiding center radius. This is shown in Figure 17.

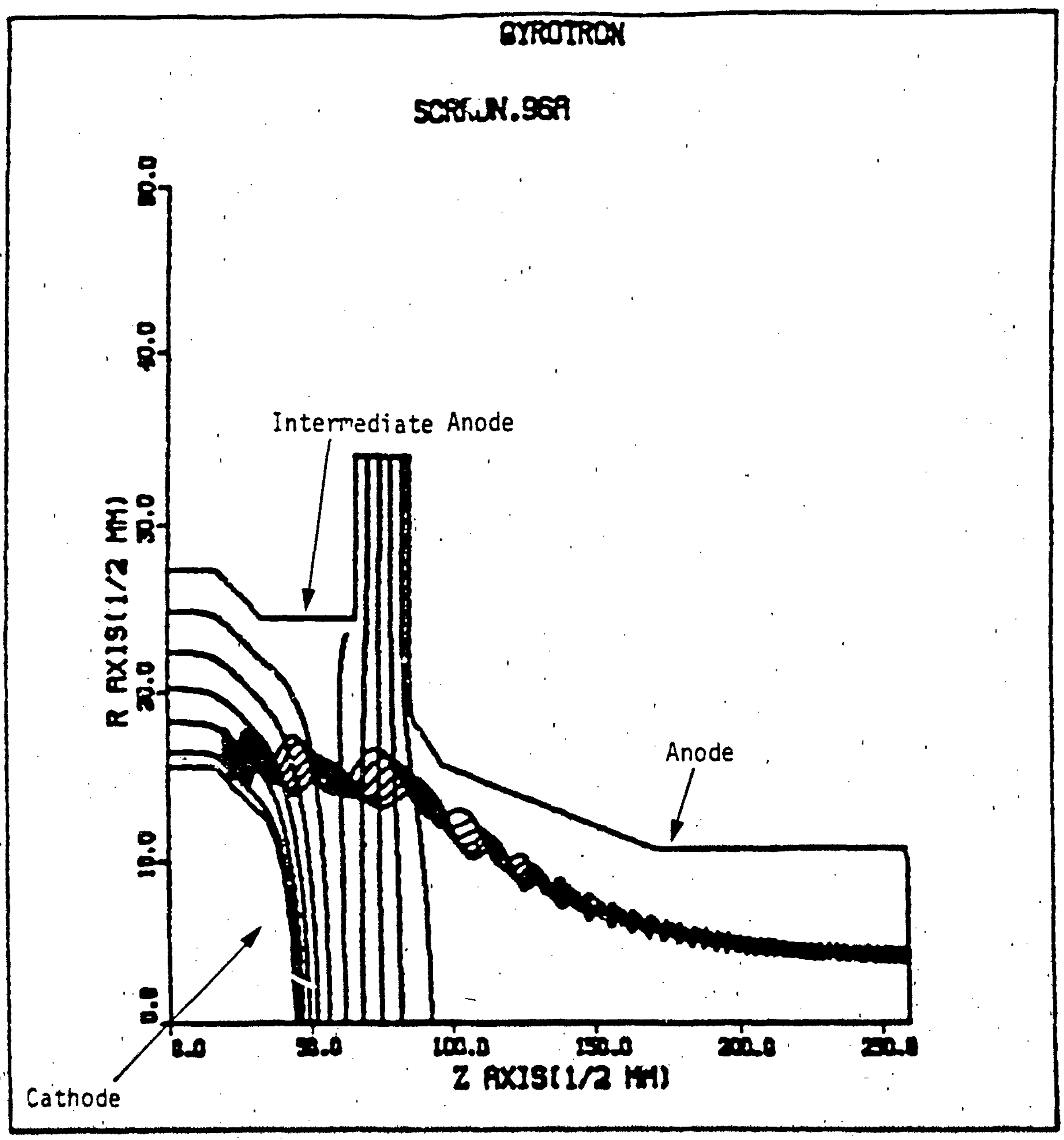

Figure 6. Trajectories and Equipotentials: Run 96

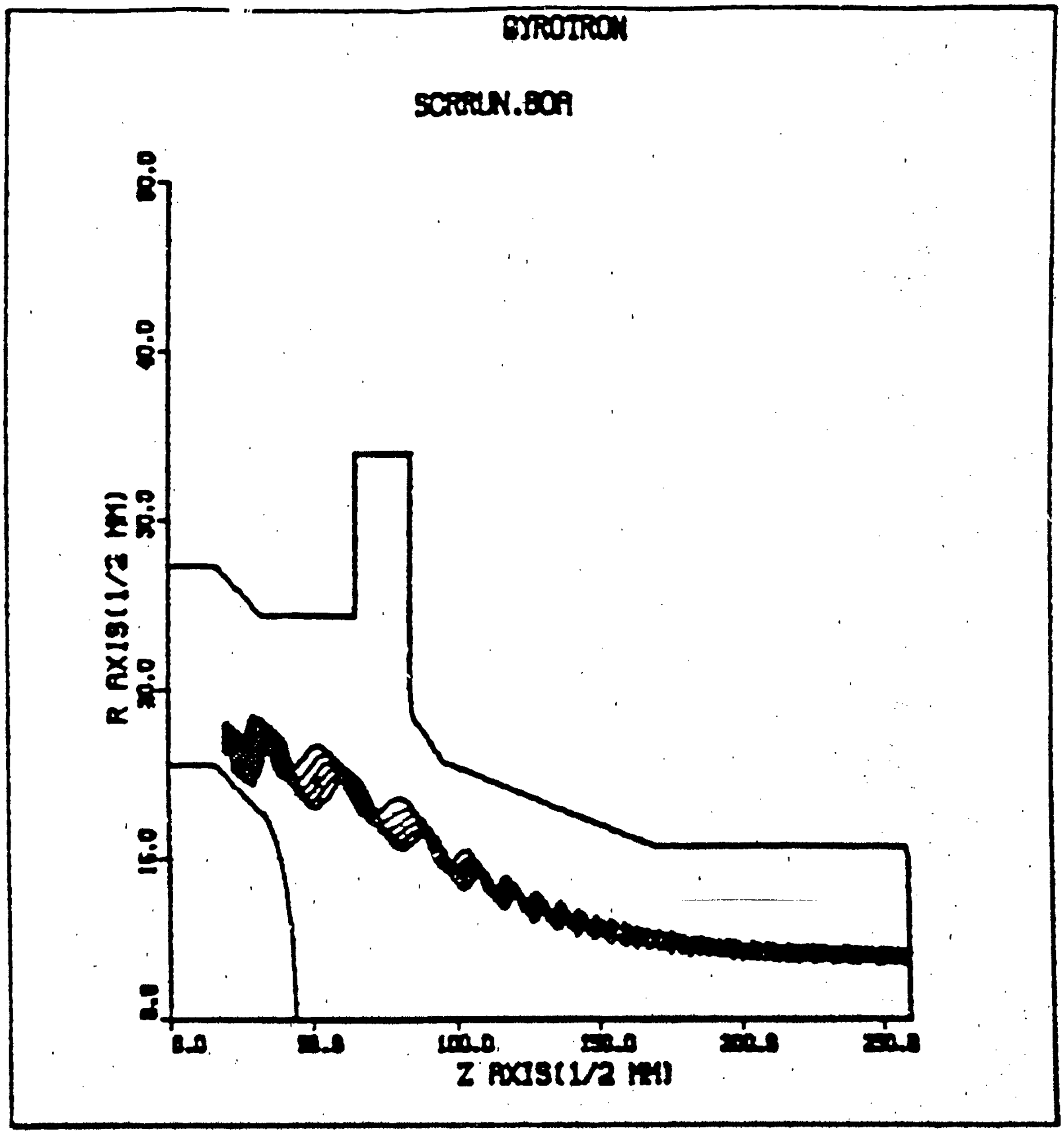

Figure 9. Trajectories: Run 80

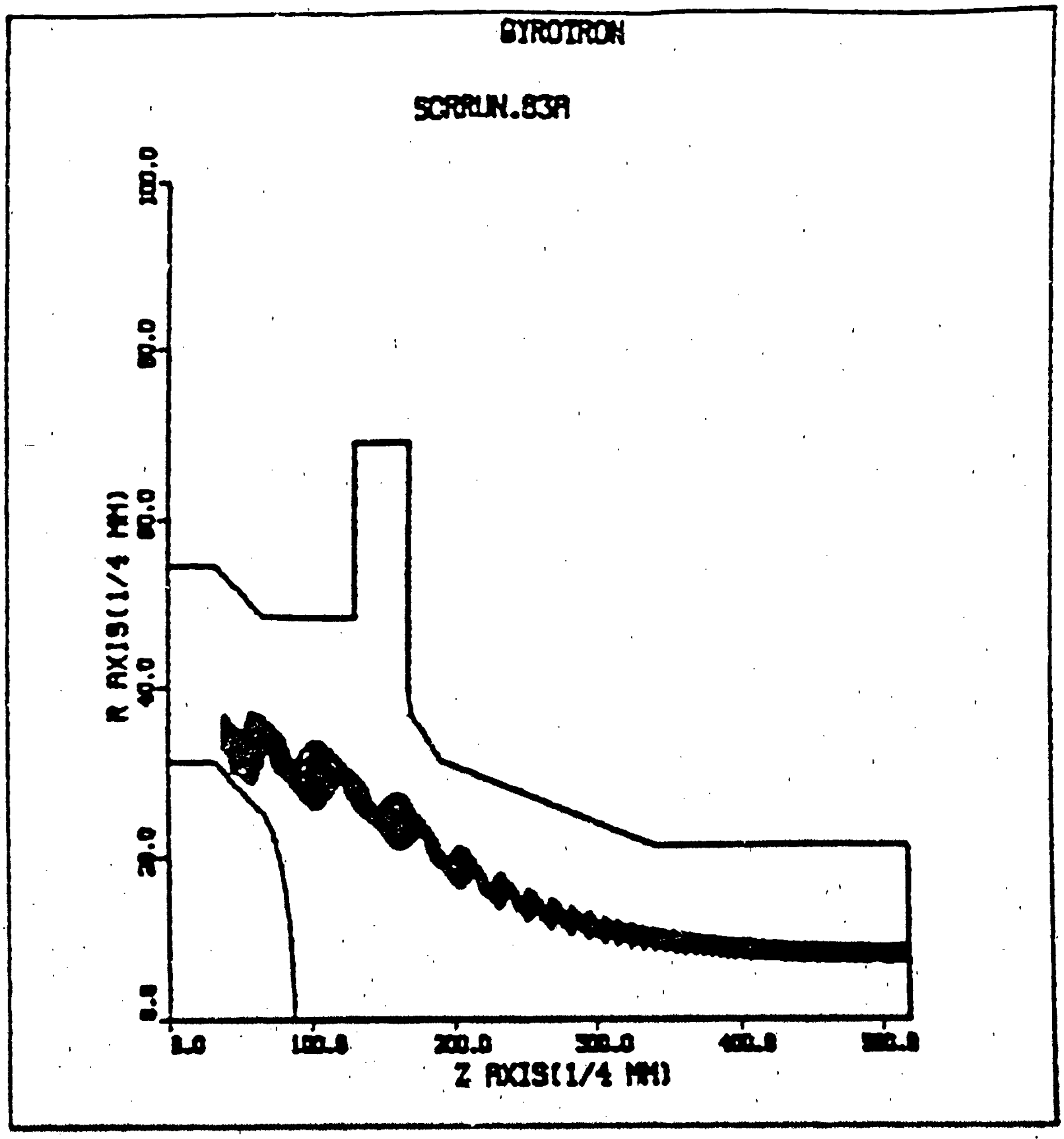

Figure 10. Trajectories: Run 83

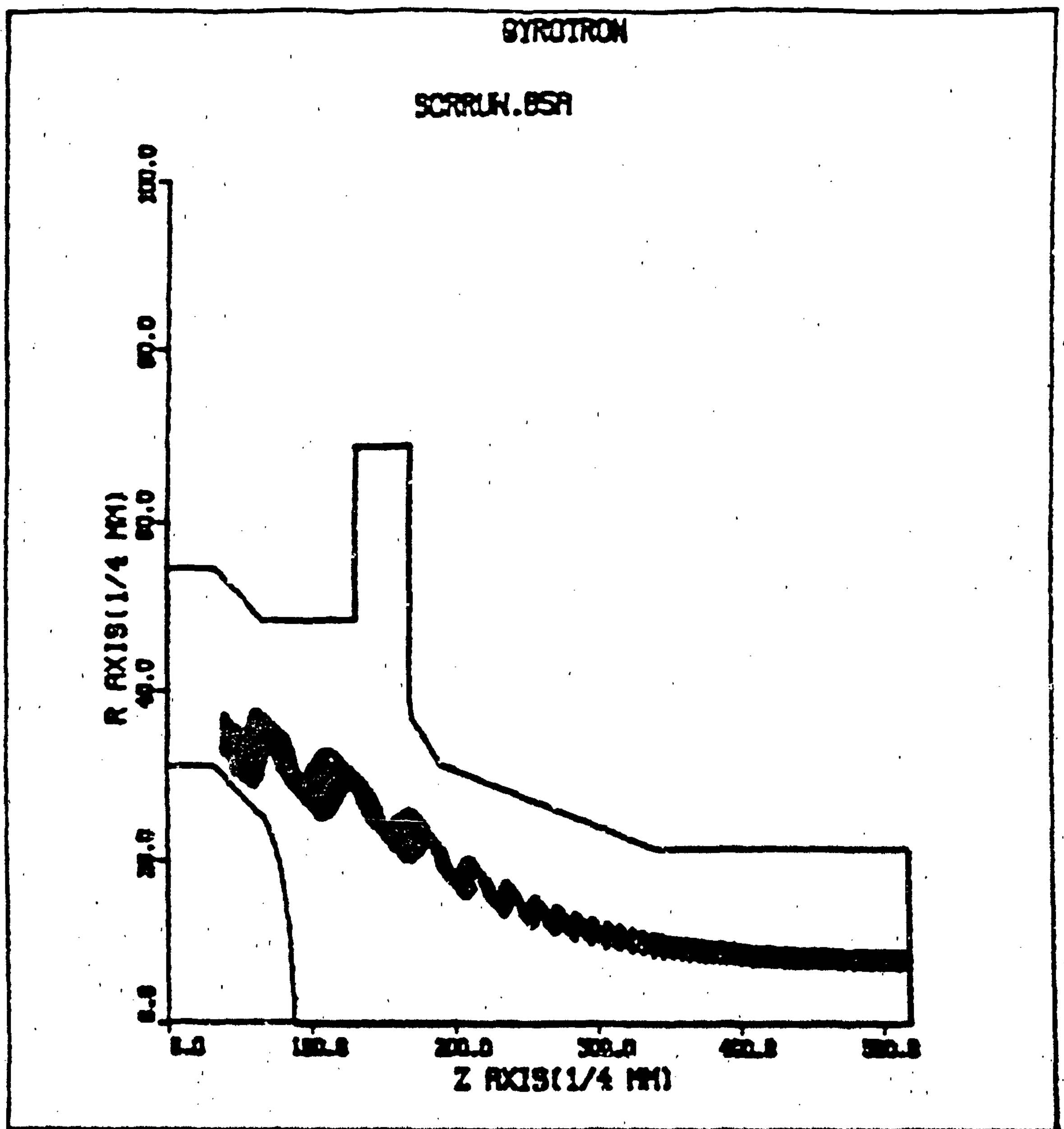

Figure 11. Trajectories: Run 85

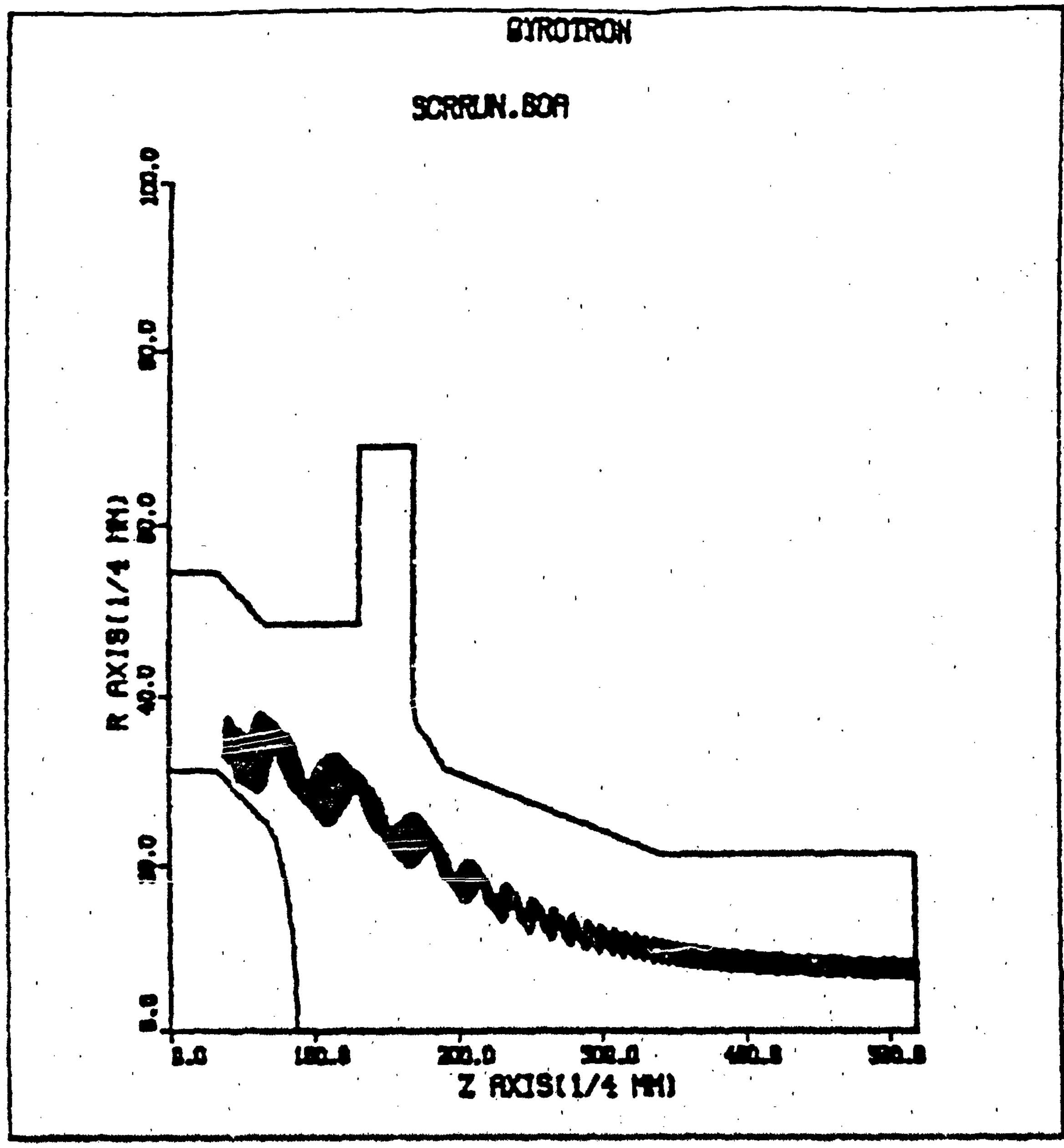

Figure 12. Trajectories: Run 60

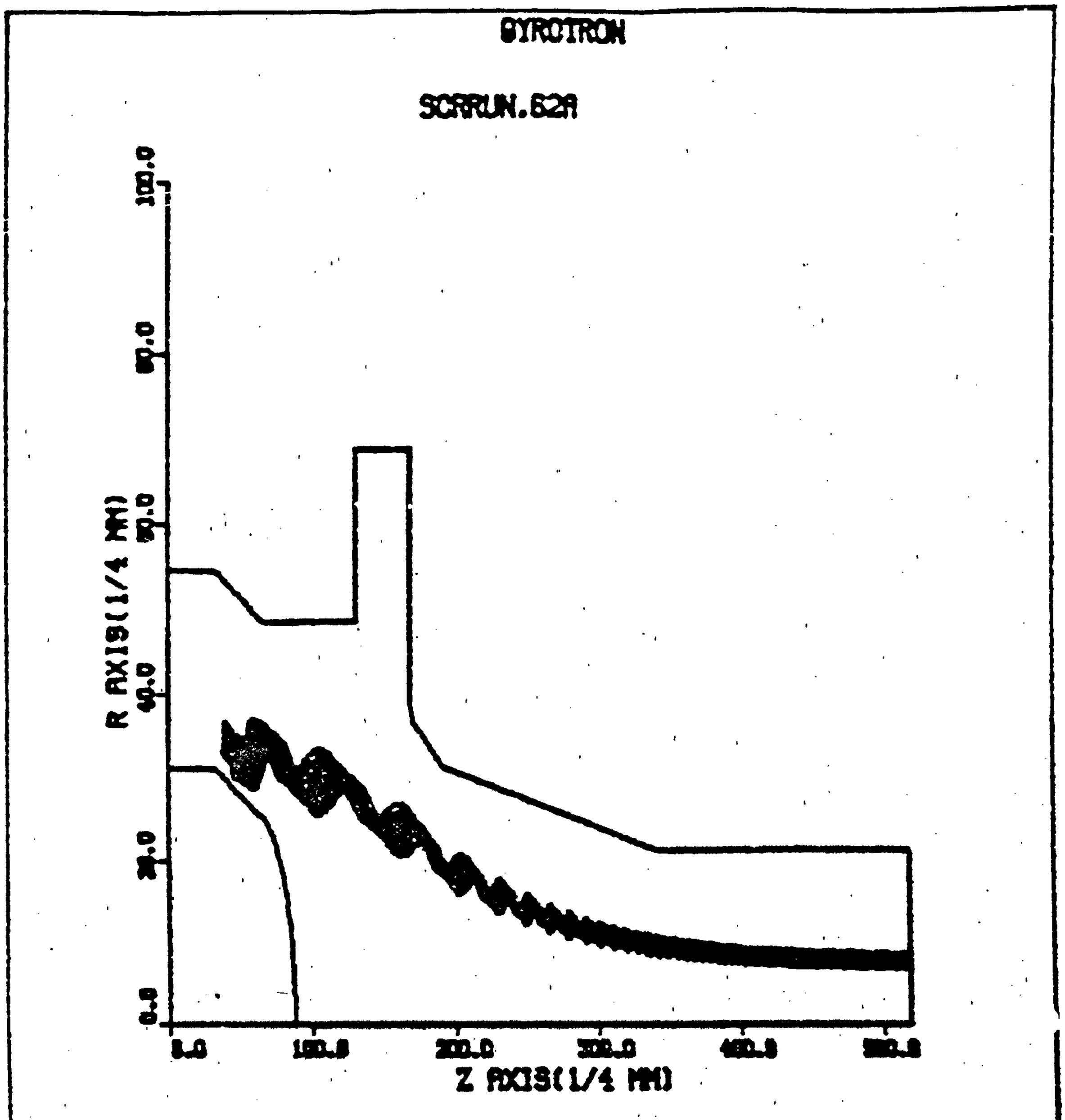

Figure 13. Trajectories: Run 62

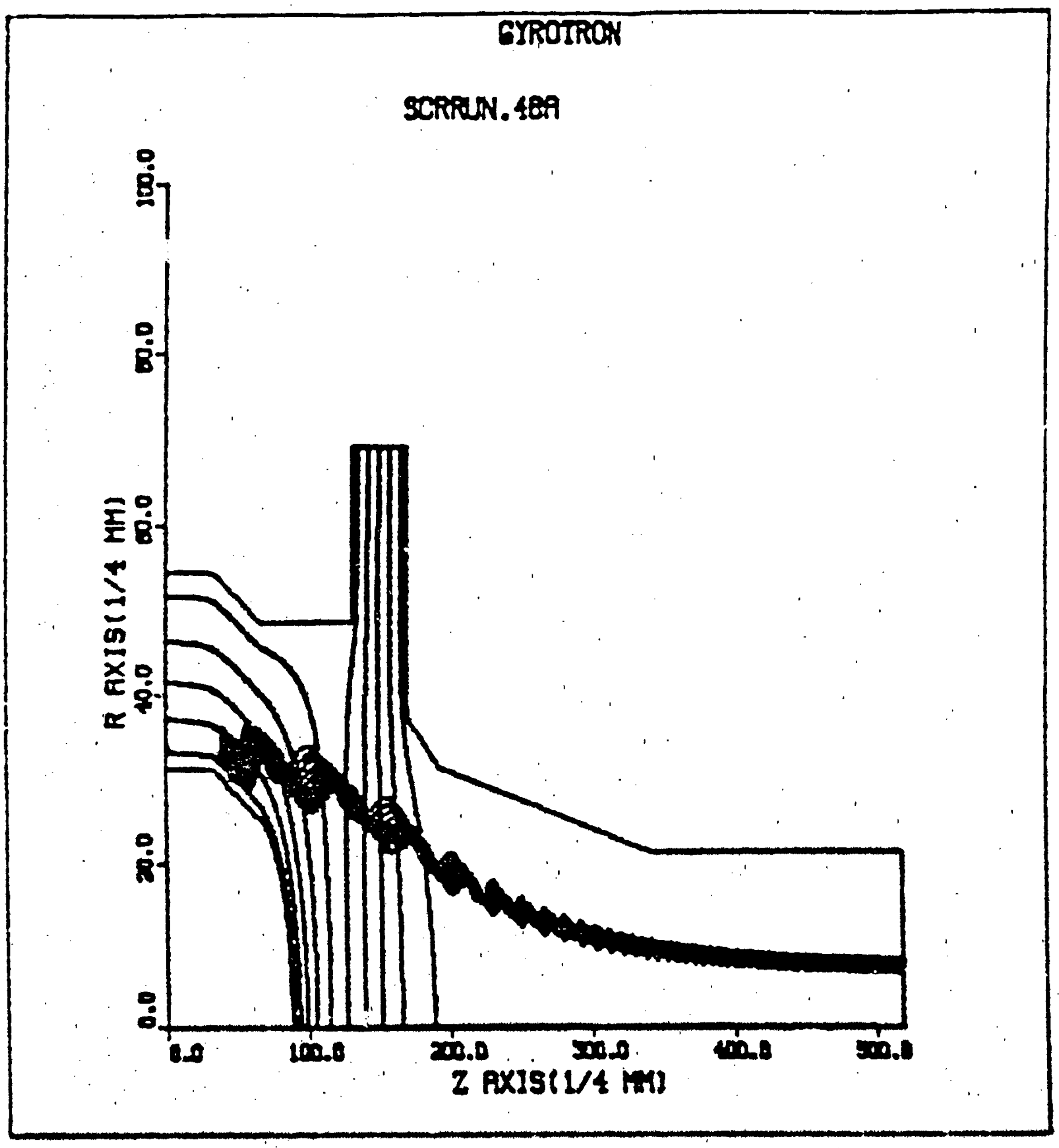

Figure 14. Trajectories and Equipotentials: Run 48

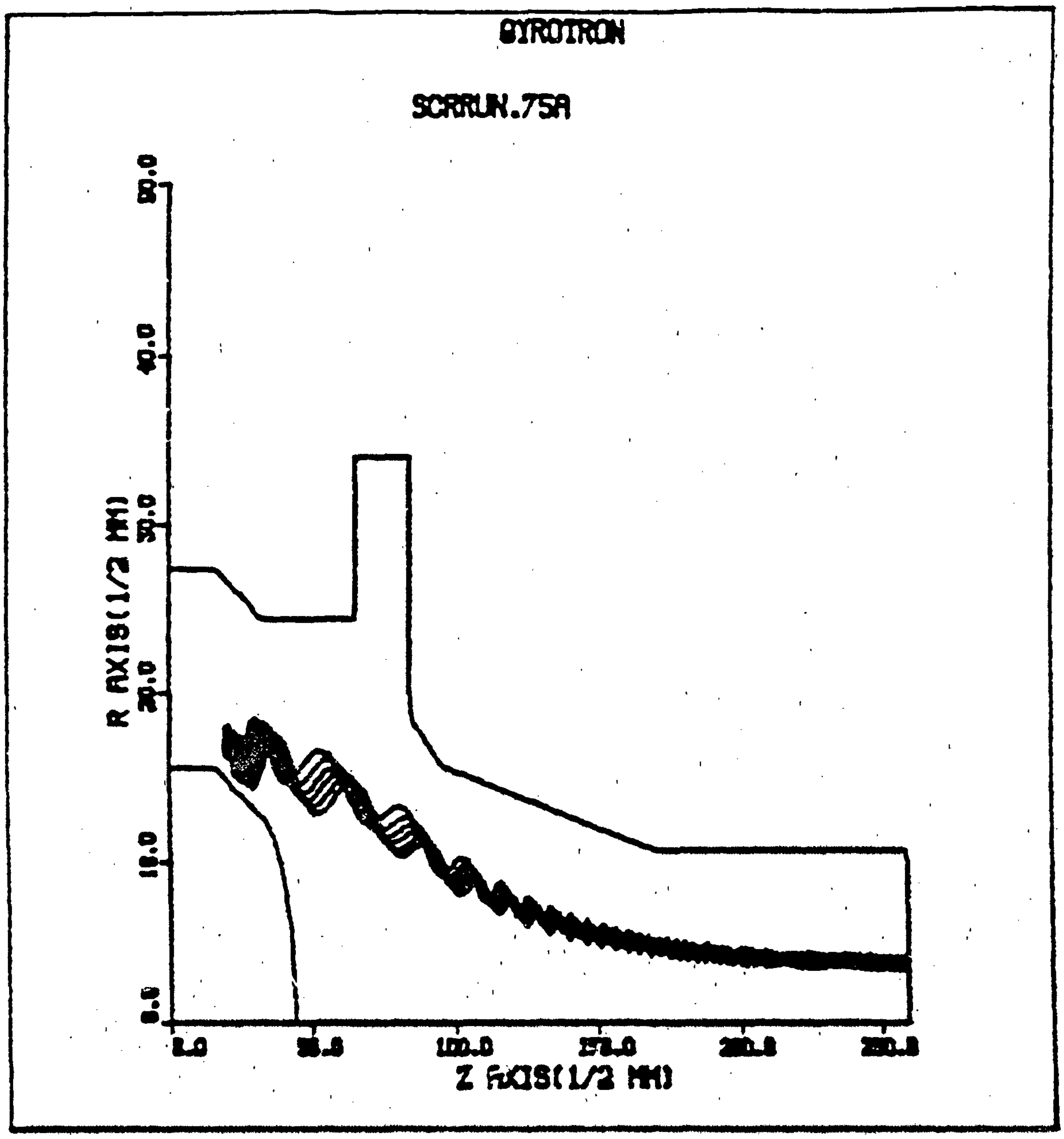

Figure 15. Trajectories: Run 75

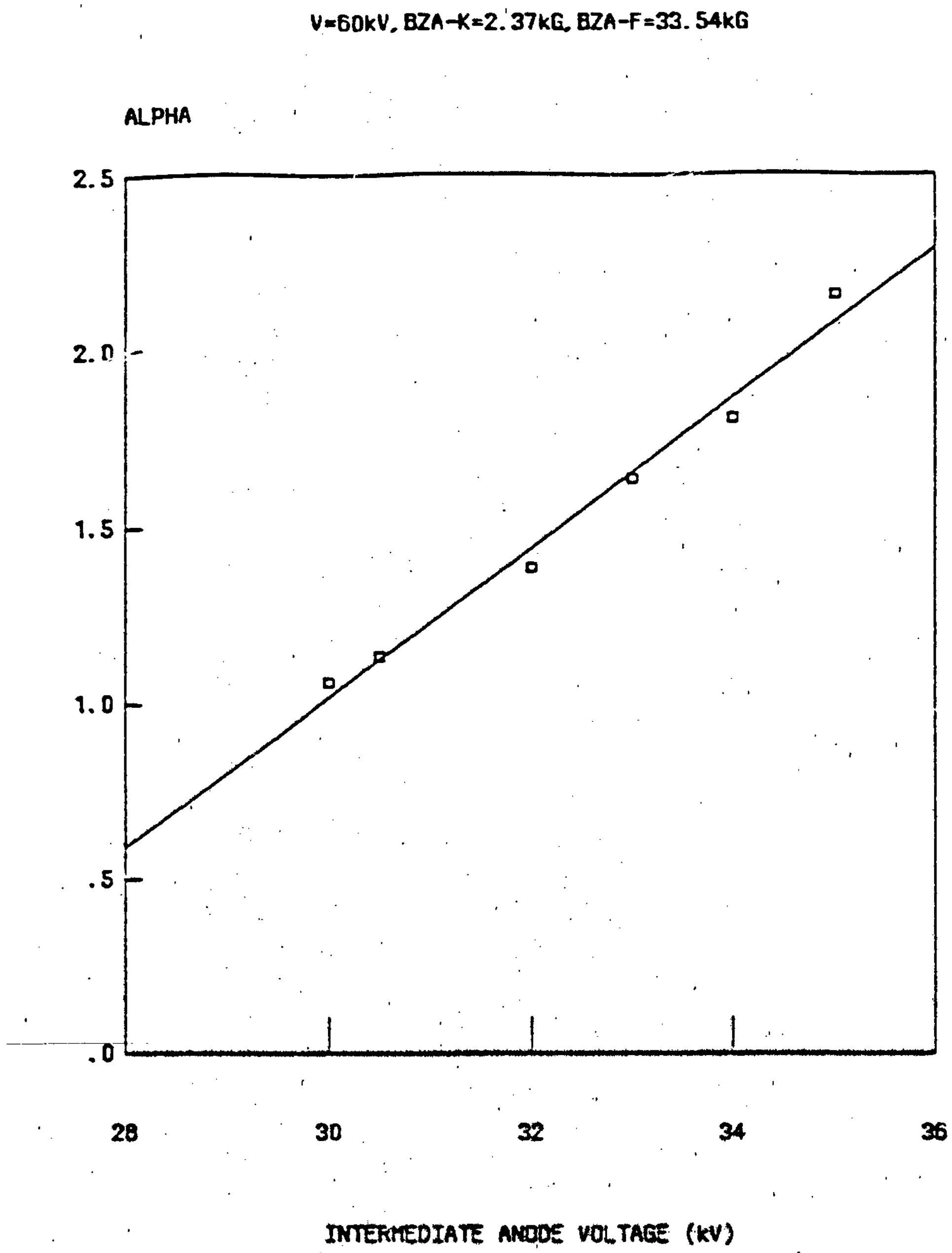

Figure 16. ALPHA Scaling with Intermediate Anode Voltage

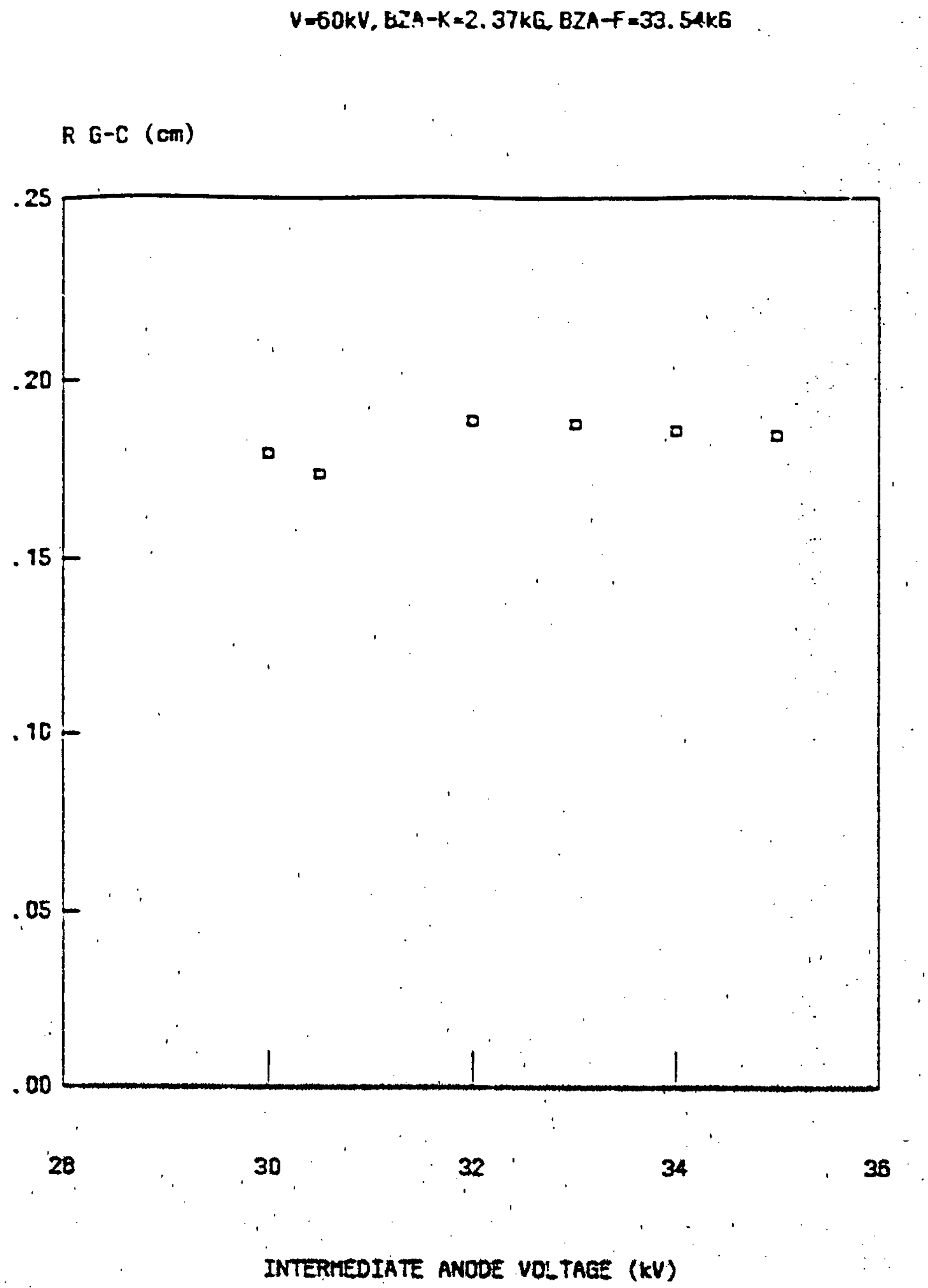

Figure 17. Guiding Center Radius Scaling with Intermediate Anode Voltage

A convenient experimental parameter, however, is the magnetic field at the cathode. Figure 18 shows the scaling of alpha with cathode magnetic field for two different anode/intermediate anode voltage settings, 67kV/35kV and 60kV/35kV. The spread in beta (parallel velocity/speed of light) for the former case is shown in Figure 19.

In summary, a number of simulations of gyrotron electron gun performance under a given set of conditions have been made. The results of these simulations have shown that several possible operating points do exist, and that the operating conditions vary approximately linearly for relatively small changes in the typical operating parameters.

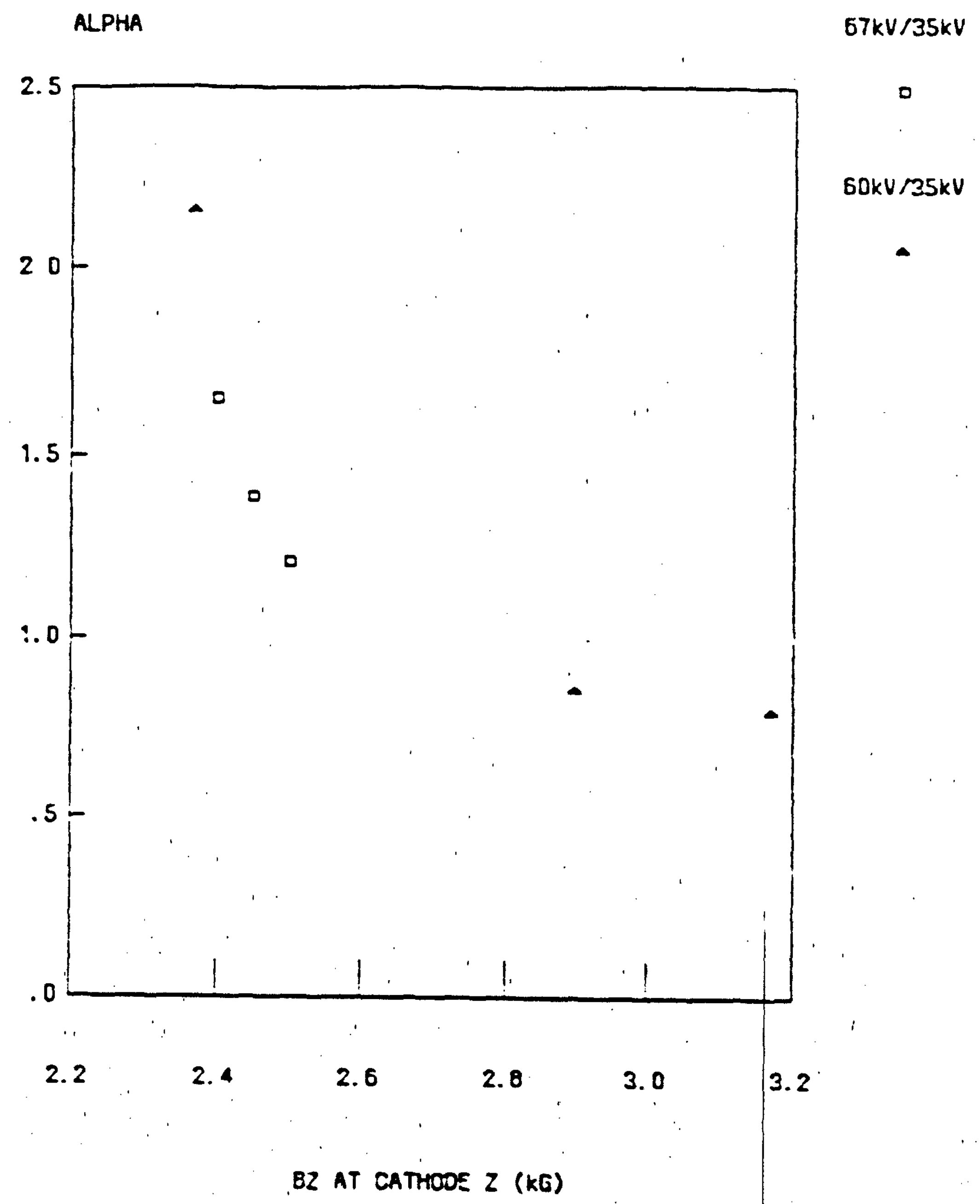

Figure 15. ALPHA Scaling with Cathode Magnetic Field

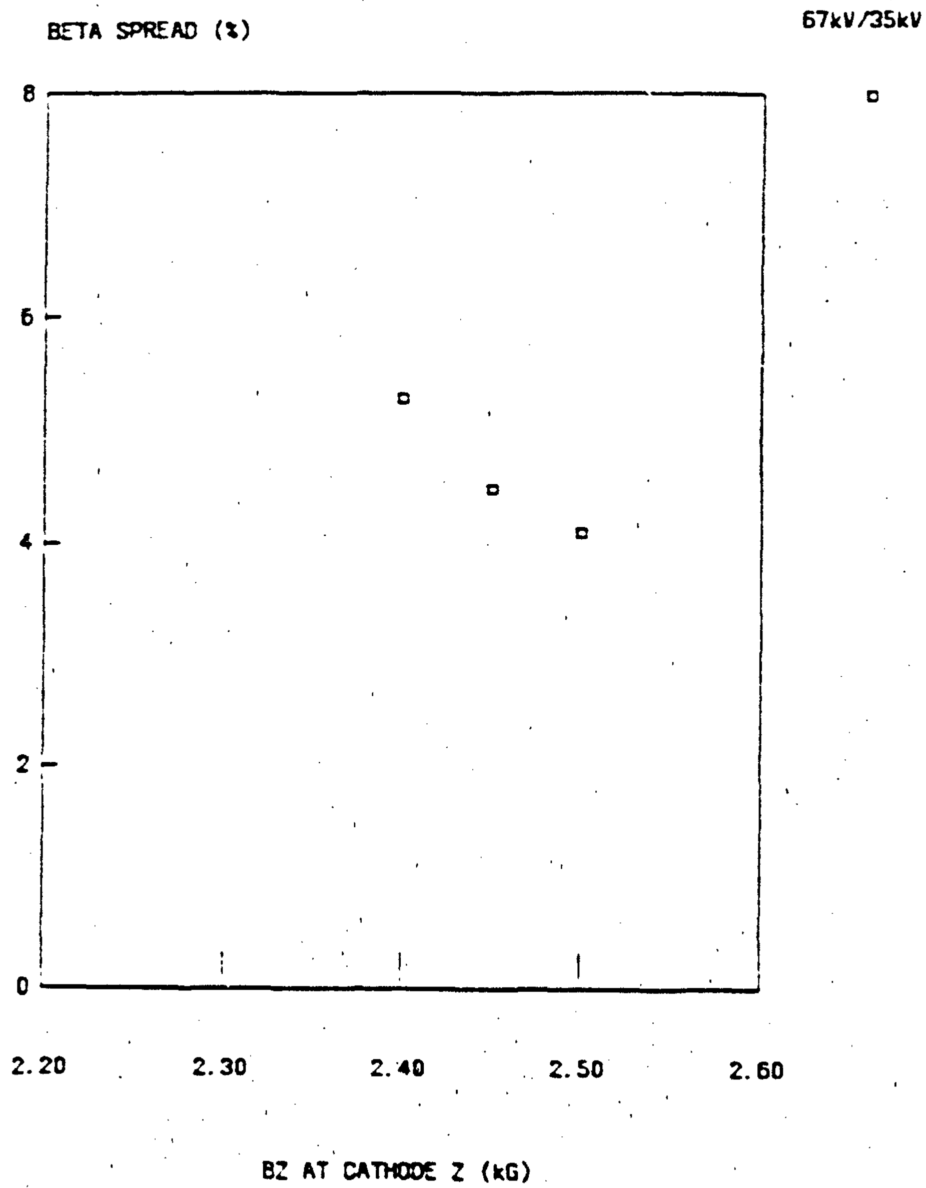

Figure 19. Velocity Spread Scaling with Cathode Magnetic Field

REFERENCES

1. A. D. MacDonald, Microwave Breakdown in Gases, Wiley, New York, 1966.

2. This technique is also used to investigate plasma-enhanced thermal coupling to metal surfaces by T. J. Wieting, J. L. DeRosa and M. E. Read in a parallel program.

3. C. L. Yee and A. W. Ali, "Microwave Energy Deposition, Breakdown and Heating of Nitrogen and Air," NRL Memo Report, No. 4617, 1981.

4. W. W. Salisbury and W. Flynt, "Microwave Energy Coupling Through Re-entry Plasma.," Varo, Inc., RADC-TR-64-575, December 1964.

5. W. Beust and W. L. Ford, Microwave Journal, 4(10), p. 91, 1961.

6. Y. P. Raizer, Sov Phy JETP, 34, p. 114, 1972.

7. W. E. Scharfman, W. C. Taylor, and T. Morita, IEEE-Trans. Antennas Propag., 12, p. 709, 1964.

8. M. E. Read, R. M. Gilgenback, R. Lucey, K. R. Chu, A. T. Drobot, "Spatial and Temporal Coherence of a 35 GHZ Gyromonotron Using the TE_{01} Circular Mode," IEEE Trans. Microwave Theory Tech., 28, p. 875, 1980.

9. W. R. Ott, P. Fieffe-Prevost, and W. L. Wiese, Appl. Opt. 12, p. 1618, 1973.

10. C. R. Barber, J. Sci. Instrum., 23, p. 238, 1946.

11. H. R. Griem, Plasma Spectrostrophy, McGraw-Hill, New York, 1964.

12. M. Imami and W. Brost, J. Chem Phys., 61, p. 1115, 1974.

13. R. M. St. John, F. L. Miller, and C. C. Lin, Phys. Rev. A, 134, p. A8885, 1964.

14. R. Nichols, Ann Geophys., 20, p. 144, 1964.

15. W. L. Wiese, M. Smith, and B. M. Glenn, "Atomic Transition Probabilites," Vol. 1, National Bureau of Standards Reference Data Systems (NSRDS-NBS-4), 1966.

16. P. Millet, Y. Salamero, H. Brunet, J. H. Galy and D. Blanc, J. Chem. Phys., 55, p. 5539, 1973.

17. W. M. Bollen, R. H. Jackson, B. Goplen, R. J. Barker, R. E. Clark, J. McDonald, C. Sedlak, "Computational Capabilities For Microwave Applications," MRC Report MRC/WDC-R-080, March 1984.

18. M. E. Read, private communication.

19. S. J. Sackett, "EFFI - A Code for Calculating the Electromagnetic Field, Force, and Inductance in Coil Systems of Arbitrary Geometry," Lawrence Livermore Laboratory Report, UCRL-52402, March 1978.

END

FILMED

10-85

DTIC